Master's thesis

NTNU
Norwegian University of Science and Technology
Faculty of Engineering
Department of Civil and Environmental Engineering

Marko Piitu Eemeli Kurttila

Borehole thermal energy storage as a seasonal capacitor in the off-grid Arctic energy supply system

Master's thesis in Cold Climate Engineering
Supervisor: Rao Martand Singh (NTNU)
Co-supervisor: Thomas Ingeman-Nielsen (DTU), Aleksey Shestov (UNIS)

July 2021

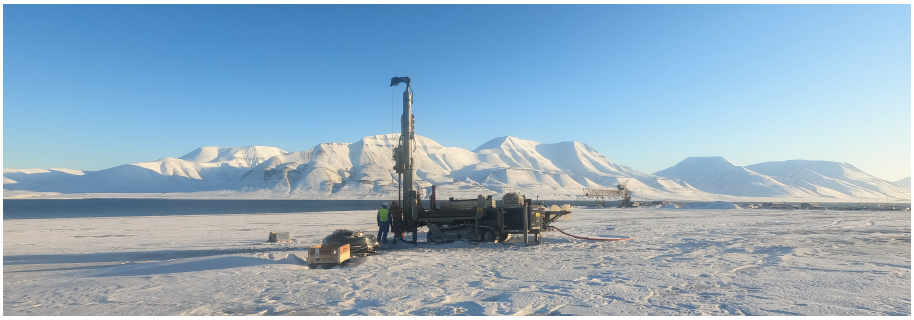

NTNU
Norwegian University of Science and Technology

DTU UNIS The University Centre in Svalbard
Cold Climate Engineering

Marko Piitu Eemeli Kurttila

Borehole thermal energy storage as a seasonal capacitor in the off-grid Arctic energy supply system

Master's thesis in Cold Climate Engineering
Supervisor: Rao Martand Singh (NTNU)
Co-supervisor: Thomas Ingeman-Nielsen (DTU), Aleksey Shestov (UNIS)
July 2021

Norwegian University of Science and Technology
Faculty of Engineering
Department of Civil and Environmental Engineering

NTNU
Norwegian University of
Science and Technology

Preface

This master thesis is the final part of studies in Land Track of the Nordic Master in Cold Climate Engineering, which is a joint programme between the Technical University of Denmark and the Norwegian University of Science and Technology. The work was carried out at University Center in Svalbard during the spring semester of 2021. Fieldwork was conducted in collaboration with Longyearbyen Lokalstyre and companies Asplan Viak, Øslandet Brønn og Energiboring and LNS.

Longyearbyen, 2021-07-16

Marko Piitu Eemeli Kurttila

Acknowledgment

First of all I would like to thank my supervisors Aleksey Shestov, Rao Martand Singh and Thomas Ingeman-Nielsen for their knowledge and guidance.

Fieldwork was carried out in co-operation with a fellow master student, Kjersti Buraas Snoen, companies Asplan Viak, LNS, Øslandet Brønn og Energiboring and the Longyearbyen local government. I would like to express my gratitude to Kjersti, Randi Kalskin Ramstad, Rasmus Bøckman, Lars and Trond for their advice and expertise shared during and after the fieldwork.

I also want to thank UNIS for providing the topic, and resources for carrying out this work. Acknowledgements to all of the staff at the technology department, logistics and geology department for helping me on my journey.

I would also like to thank my fellow students for their support for my thesis work, in and out of office. Thank you Sarah Heller and Renato Rodrigues for an amazing spring. I also want to thank my family and friends who have supported me even from the other side of the world.

Finally I want to express my gratitude towards everybody that is not mentioned here and that has provided me with support on my journey. Thank you.

M.P.E.K.

Summary and Conclusions

This master thesis investigated the feasibility of borehole thermal energy storage and solar heating in the high arctic using Longyearbyen in Svalbard as a reference study place. Field work was conducted in Longyearbyen, Svalbard to estimate thermal properties of ground. Modelling of the energy storage was conducted to estimate the efficiency and environmental impact. Preliminary cost estimate was conducted to determine the economical feasibility of the technology in the Arctic. Results of this thesis concluded that the borehole thermal energy storage is technologically possible in the Arctic environment. Cost estimate for the system appears to be in the higher range, but not extraordinary high when compared to energy prices worldwide. Main concerns related to implementing this technology is the thawing of permafrost.

Contents

List of Figures

List of Tables

Nomenclature

Acronyms

- 1D - One Dimensional
- 2D - Two Dimensional
- 3D - Three Dimensional
- ASHRAE - American Society of Heating, Refrigerating and Air Conditioning Engineers
- ATES - Aquifer Thermal Energy Storage
- BTES - Borehole Thermal Energy Storage
- BTES-HT - High Temperature Borehole Thermal Energy Storage
- CAD - Computer-aided Design
- CAPEX - Capital Expenditure
- CHP - Combined Heat and Power
- CHTM - Constant Heating Method
- COP - Coefficient of Performance
- DTH - Down The Hole
- DTRT - Distributed Thermal Response Test
- DTS - Distributed Thermal Sensing
- GHE - Geothermal Heat Exchanger
- GSHP - Ground Source Heat Pump
- GWL - Ground Water Level

- LCOE - Levelized Cost of Energy
- LNG - Liquefied Natural Gas
- LSM - Line Source Method
- MAAT - Mean Annual Air Temperature
- NGU - Geological Survey of Norway
- OPEX - Operational and Maintenance Expenses
- OPEX - Operational and Maintenance Expenses
- PE-RT - Polyethylene of Raised Temperature
- PF - Permafrost
- PTES - Pit Thermal Energy Storage
- PV - Photovoltaic
- TCT - Thermal Cone Dissipation Test
- TES - Thermal Energy Storage
- TRT - Thermal Response Test
- TRTWD - Thermal Response Test While Drilling
- UNIS - University Centre in Svalbard
- UTES - Underground Thermal Energy Storage
- XRD - X-Ray Diffraction
- eTRT - enhanced Thermal Response Test
- m.a.s.l - meters above sea level

Symbols & Units

- °C - Degree Celsius
- λ - Thermal Conductivity
- CO_2 - Carbon dioxide

- GWh - Gigawatthour
- K - Kelvin (unit of temperature)
- M€ - million euros
- MW - Megawatt
- MWh - Megawatthour
- Ma - Million years
- cm - centimeter
- k€ - thousand euros
- kg - kilogram
- km - kilometer
- mW - milliwats
- mm - millimeter

Chapter 1

Introduction

1.1 Situation in Longyearbyen

Longyearbyen is the largest town in Svalbard with home to over 2,000 permanent residents and 150,000 person-days of visitors annually (Ringkjøb et al., 2020). The town is on a verge of renewing the current energy system. Some of the most important drivers for the change are:

- Longyearbyen is powered by the only coal-fired power plant in Norway. Heat and electricity in the town are produced by locally mined coal. As the government of Norway has a goal to become a low-carbon society by 2030, as stated in the white paper by Solberg government (2021), an alternative for coal combustion must be found. The current CO_2 emissions from the power plant are approximately 60,000 tons per year. (Ringkjøb et al., 2020)
- Local coal reserves are running out. The power plant in Longyearbyen utilizes locally mined coal from Mine no. 7. The mine is located in Adventdalen, a little over 10 km southeast from the town. However the coal reserves are estimated to last only for the next decade. Continuing with coal combustion would require fuel to be imported from farther away, further increasing the indirect CO_2 emissions of the society. (Ringkjøb et al., 2020)
- Age of current energy the infrastructure. The life-cycle of the current power plant is at the end. The operating power plant was recently renovated, extending the life-cycle of it until 2038. New energy system should be operating by then, in order to keep the city functioning. (Ringkjøb et al., 2020)

The energy production affects the lives of many people, and the local government has strong techno-socio-economic interest in the development of a new energy system for the town, and maybe even for the whole archipelago.

There are multiple options for alternative energy sources such as diesel, hydrogen (Brekke et al., 2018), LNG (Vartdal, 2017), geothermal energy (Midttømme, 2017), power line connection from the mainland (Moen, 2017), or wind & solar energy. One major issue with the latter option is high timely variation in the production.

This thesis investigates the possibility of using solar collectors coupled with Borehole Thermal Energy Storage to fulfill the heating demand for the town. Electricity production and consumption is not discussed in this work. Main goal of the thesis is to investigate the feasibility of the BTES in permafrost areas. Secondary object is to assess the use of solar collectors in providing district heating.

1.2 Objectives

The main objectives of this project are

1. Investigate the technological feasibility of BTES in a high arctic environment in Svalbard.
2. Assess the environmental impacts of the BTES, mainly the effect on surrounding permafrost.
3. Economical feasibility of solar heating coupled with BTES.

1.3 Approach

The technical feasibility of the BTES is investigated trough literature review, fieldwork and numerical modelling. The environmental impacts are assessed by analyzing the results from the numerical modelling. The economical feasibility of the BTES coupled with solar heating is assessed trough market research of technological costs and comparing these with the current energy prices gained by interviewing the stakeholders.

1.4 Structure of the Report

The rest of the report is structured as follows. Chapter 2 gives an overview of the relevant background information which would affect the study objectives presented in section 1.2.

This includes the local geography, geology, climate and the current energy system. Chapter 3 provides knowledge of the Borehole Thermal Energy Storage as a technology. Chapter 4 presents the fieldwork conducted as part of this thesis. The fieldwork is divided into three sections: drilling, sampling and the Thermal Response Test (TRT). It discusses the methodology, results and limitations of each subsection. Chapter 5 gives detailed information about the numerical modelling of the BTES done within this study. It explains how the model was created, and provides the results from the simulation. Chapter 6 provides economical analysis and preliminary cost for heat produced with the new system. Chapter 7 discusses the findings of this study and answers the research questions stated in the objectives.

Chapter 2

Background

2.1 Current Energy System

Longyearbyen has a combined heat and power plant (CHP) with 11 MW of electrical and 22 MW of heating capacity. The powerplant produces 40 GWh of electricity and 70 GWh of heat per annum. The power plant can be seen in figure 2.1. In addition to the main coal power plant, there is also a diesel powered backup generators. The power plant uses 25,000 tons of coal annually, and produces 65,000 tons of CO_2. The whole town is supplied with district heating. (Brekke et al., 2018)

Figure 2.1: Coal powered CHP power plant in Longyearbyen. The old power plant can be seen on the left side of the picture.

The district heating system consists of three loops, interconnected with heat exchangers.

The main distribution line runs from the power plant to heat exchanger stations which area called boiler centrals in this work (see Figure 2.2a). These stations also house boilers that allow increasing or lowering of the fluid temperature. The temperature in the main loop is between 95 and 120 °C. From the boiler stations the heat is transferred to a secondary loop which connects to so called sub-centrals. The water temperature in the secondary loop is between 73 and 90 °C. From the sub-centrals the heat is transferred to the local heating circuit for the heating and hot water production.

(a) Boiler station.

(b) District heating pipeline.

Figure 2.2: The boiler central and the main distribution line of the district heating network. The pipeline is founded on piles on top of ground to prevent permafrost thaw. The bridge is designed as an overpass for snowscooters and pedestrians.

In Longyearbyen the distribution line lies on wooden piles on top of ground due to permafrost, as seen in figure 2.2b. The main purpose of this is to prevent the permafrost from thawing, and keeping the ground close to it's natural state. In more temperate climates, the district heating network - along with most of technical installations - are buried underground. From the civil engineering perspective there are strengths and weaknesses to this approach when compared to underground installations. Advantages include lower installation costs since excavations are not needed. Due to same reasons maintenance is cheaper, and the pipeline is more easily accessed when it is on top of the ground surface. Disadvantages include higher heat losses. Variation in the intra-year ground temperature has lower amplitude than in the air temperature. Soil overburden acts as a natural insulator. This effect is amplified during winter and summer season. When the air temperature during winter reaches extreme low values, and consequently heating demand increases, the temperature difference between the district heating system and the ambient air increases, causing higher heat transfer from the pipe into the ambient air. During warm summer days this effect is reversed. On-the-ground installations also require a lot of space, which would affect land use.

2.2 Geology

Svalbard is an archipelago situated in the Arctic sea, approximately halfway between the North Pole and mainland Norway (see figure 2.3). Longyearbyen is the administrative capital of Svalbard, situated at the southwestern shore of the Adventfjorden on the island of Spitsbergen, shown in figure 2.4.

Figure 2.3: Map of the Arctic sea. Svalbard encircled in red. Source: CIA World Factbook (2021)

Figure 2.4: Summer satellite image from Longyearbyen and Adventfjorden. Source: Norwegian Polar Institute (2021)

The whole archipelago of Svalbard was - and by some countries is still - called Spitsbergen. The word originates from Dutch, meaning pointy mountains. The reasoning behind the name can be seen especially along the western coast, showing high relief and sharp mountain tops. The topography of Svalbard is dominated by mountains, fjords, U-valleys and glaciers. The mountain types can be further divided into three geomorphological classes. According to Dallmann (2015) these are: 1) Rounded mountains, 2) Plateau mountains and 3) Edged Alpine mountains.

The landscape around Longyearbyen is mainly Plateau mountainous landscape area. This is clearly seen in Figure 2.7 showing the flat surface of the Platåfjellet mountain. Majority of the town is located in a U-valley. The airport lies on a coastal lowland, and Adventdalen, to the south-east is one of the largest U-valleys on the island. Different landscape classifications near Longyearbyen can be seen in figure 2.5.

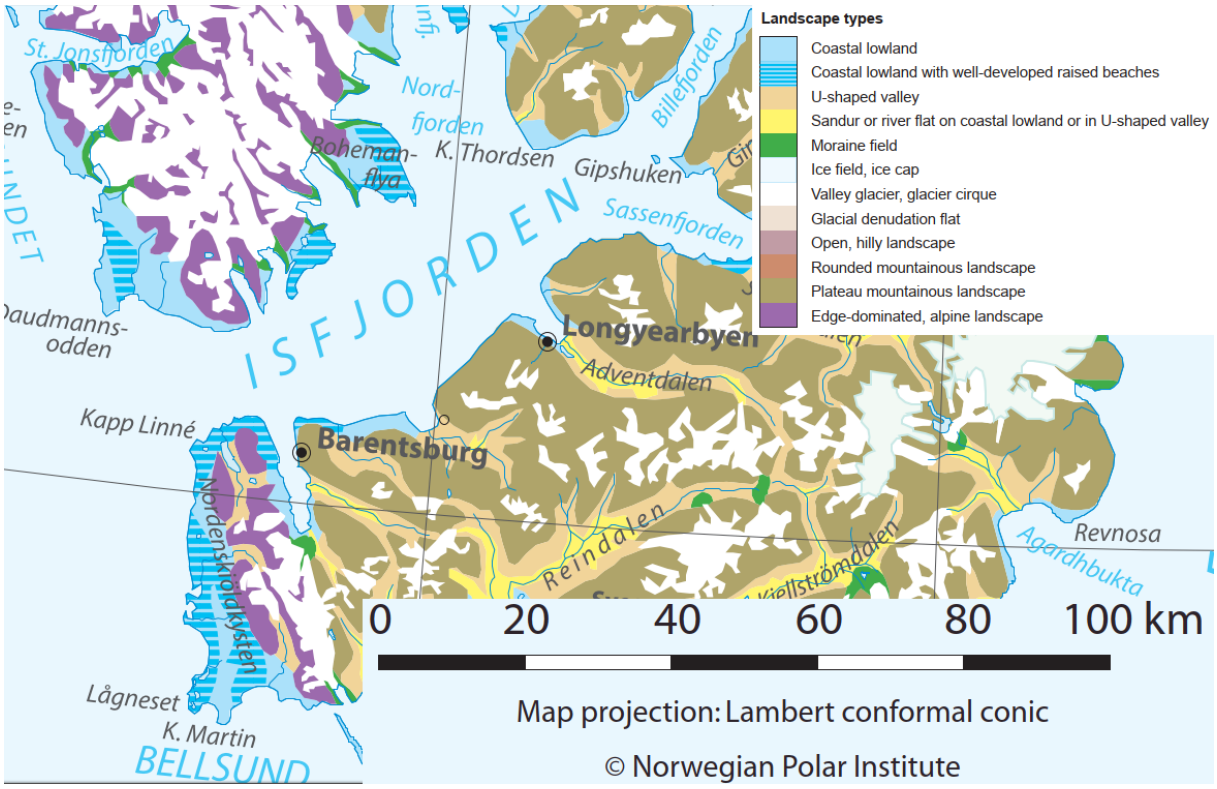

Figure 2.5: Map of landscape types of Svalbard. Source: Dallmann (2015)

Glaciers

Glaciers form in areas where the yearly accumulation of snow is higher than the amount depleted. Majority of this happens through snowfall and melting. Other processes which affect the glacier mass balance are snow drift, sublimation and calving especially in glaciers terminating in water. Over long time span (up to thousands of years) the accumulated snow pack gets thicker. The weight of the overlaying snow compresses the snow layers deeper within the snow pack, compressing it until it turns into ice. Once the weight of the glacier grows high enough, it starts to deform and flow downwards. (Souchez and Lorrain, 1991)

Approximately 59 % of the land area in Svalbard is covered in glaciers. The amount of glacial ice on the archipelago has varied during the past tens of thousands of years. The Last Glacial Maximum occurred approximately 24,000 years ago, and the last glacial minimum in 7-8,000 years ago. Due to the recent retrieval of glacial ice, the land masses in Svalbard have experienced post-glacial isostatic uplift. This is a phenomenon, which is born when a high amount of ice causes gravitational forces pushing the earth's crust downwards into the mantle. During glacial maximums, a lot of the water on earth is bound in glaciers, thus the oceans tend to be at a lower level. Decreasing glacier mass, for example due to climate warming, happens relatively fast (in geological time-perspective) causing the sea level to

rise. However due to high viscosity the elastic rebound in the mantle of earth happens a lot slower. Before and at the start of this upheaval process, marine sediments will be deposited on the sea-floor, which eventually rises above the current mean sea level. (Dallmann, 2015)

Svalbard is a large area with very few inhabitants. However most of the land area is covered in glaciers and mountains. This limits the possible locations for BTES or other related infrastructure.

Sedimentary deposits

In Svalbard, marine sediments can be typically found on low elevations. On the west coast these are up to 65 meters above sea level (m.a.s.l.), but on Kongsøya up to 110 m.a.s.l. (Dallmann, 2015). According to L. Gilbert et al. (2019) the level is 60-70 m.a.s.l. near Longyearbyen. These marine sediments are typically sand and/or gravel (beach type) or mud (lagoon type) (Dallmann, 2015). Marine sediments have tendency to exhibit salinity (L. Gilbert et al., 2019), but the if sufficient groundwater flow is occuring in the sediment layer, most of this salinity might have been leached away possibly forming so called quick clay. This might be a potential geohazard, which should be considered. Salinity also causes freezing point depression (Harstad et al., 2018), which will also affect permafrost stability by causing the permafrost to thaw at lower temperatures than 0°C.

Other soil types within Longyearbyen include fluvial and deltaic deposits, especially in Adventdalen (L. Gilbert et al., 2019). Field investigation report by Stover (2019) records residual soil around the current power plant and soundings by Nårstad et al. (2018) shows till near the town center. The thickness of the sedimentary deposits above the bedrock surface varies significantly from 0 meters on the bedrock outcrops to over 20 meters near the town center. Soundings made down to 24 meters depth by Nårstad et al. (2018) did not encounter bedrock. Near the river by the new Elvesletta student housing, bedrock has been reported at 28 meters depth (Pedersen and Bæverfjord, 2018).

Bedrock

The bedrock nearby Longyearbyen consists of 60 to 66 Ma old Danian deposits higher on the mountains (Harstad et al., 2018), and 100 to 125 Ma old Aptian-Albian deposits closer to the sea level. The major rocktypes are layered shale- , silt- and sandstone. There are thin coal seams in the Paleocene Firkanten formation (Dallmann, 2015). This is the formation where the local coal is mined. The drill site (discussed in chapter 4) is located on the Carolinefjellet

formation, consisting of sandstone and shale layers (2.6). Sandstone generally consists of quartz minerals, which have relatively high thermal conductivity, making it suitable thermal storage medium.

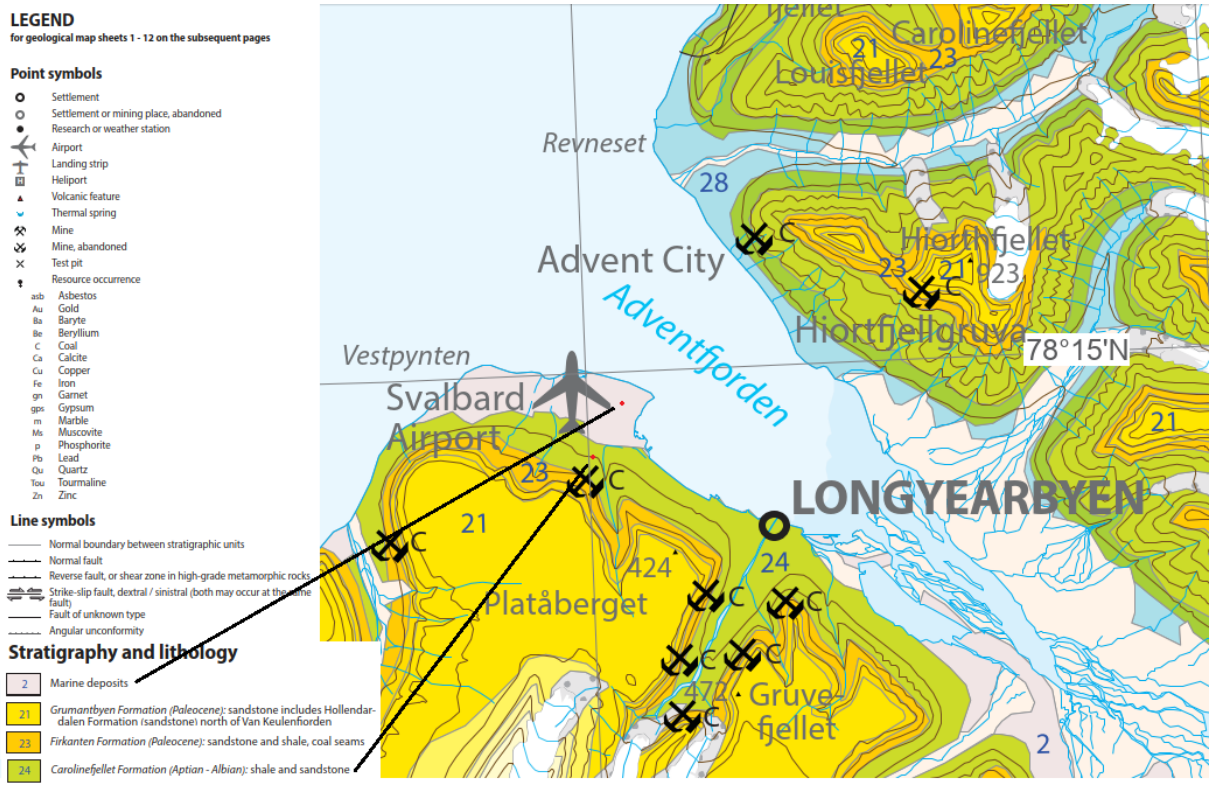

Figure 2.6: Geological map of Longyearbyen are. Red dots indicate the drill sites. Source: Dallmann (2015)

According to Harstad et al. (2018) the upper 4 to 8 meters of bedrock can be heavily weathered and cracked due to frost expansion. The weathering and erosion can be clearly seen on the toes of the rock slopes when walking around Longyearbyen. This can be seen in figure 2.7. These cracks and fissures will also increase drainage abilities if the permafrost thaws.

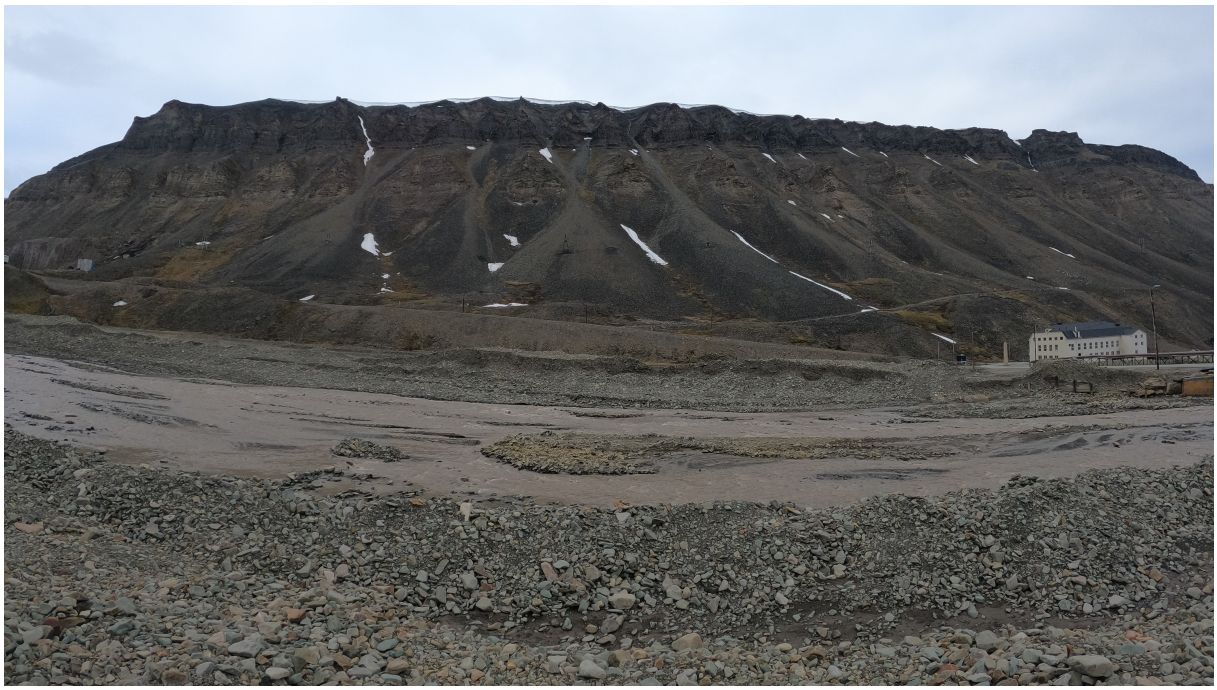

Figure 2.7: Picture of Platåfjellet taken from Longyeardalen. Alluvial/debris flow can be seen as fan shaped deposits on the mountain slopes. Fluvial deposits can be seen on the foreground by the riverbed.

Dorval (2020) investigated mechanical properties of local rock materials to assess if that could be used as a construction material. The results from the Micro-Deval abrasion tests were at a high level, meaning that the local rock is sensitive to wear. However even more importantly the results obtained from Los Angeles test, which is useful in identifying brittle materials with tendency to break on impact, showed intermediate level. According to these results the local rock could be classified as relatively weak in mechanical perspective. Brittleness is correlated with higher drilling advance rate, which may lower the drilling time and drill bit wear, subsequently lowering the construction costs of the BTES.

The Norwegian Geological Survey (NGU) has conducted borehole logging from wells Dh1 and Dh2 near the shoreline on the road between Longyearbyen and airport. The boreholes were drilled as a part of "CO2 project" and the results can be found in NGU report 2008.054 by Elvebakk (2008). The logged parameters included temperature, conductivity, natural gamma, resistivity, seismic velocity, caliper, density (qualitative) and deviation. Porosity can be estimated from the resistivity data. The porosity ranges between 2 and 13 % and is illustrated in figure 2.8 by Braathen et al. (2012).

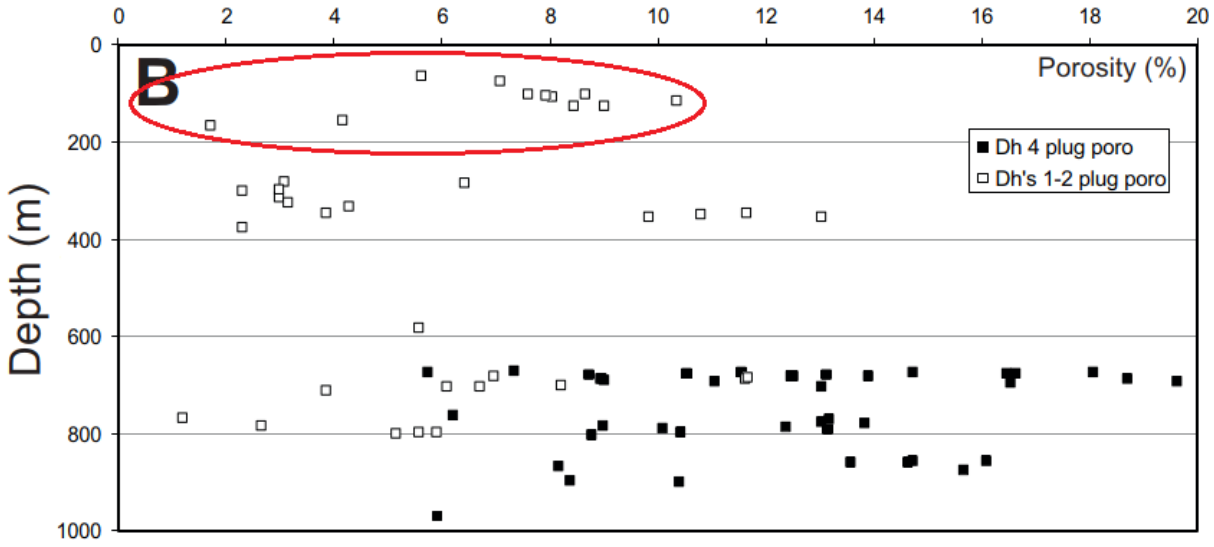

Figure 2.8: Porosity from the CO2 project. The most relevant data circled. Source: Braathen et al. (2012)

Permafrost

Permafrost is ground which stays frozen for at least two consecutive years. Permafrost is divided into continuous, discontinuous and sporadical depending on the extent (Davis, 2001). Area is classified as continuous permafrost if at least 90% of the area is covered in permafrost. Unfrozen ground can still be found in permafrost areas. These unfrozen parts are called Taliks, and can typically be found near water bodies such as lakes (Harris et al., 2018). Over 20% of the land area in the whole world is covered in permafrost. Most of this is in the Siberia, Canada, Alaska, China and Greenland but there are also Alpine permafrost in high elevations found in Scandinavia, Tibetan plateau and the Himalayas, Andes and multiple other places. Millions of people live within permafrost areas (Ramage et al., 2021) and major economical activities such as oil & gas and mining industries operate in PF areas.

Ground surface in Svalbard is covered in continuous permafrost. Active layer is the uppermost part of permafrost which experiences seasonal thaw and refreezing - analogical to seasonal frost depth in warmer climates. The thickness of the active layer in Svalbard is typically 0.5 - 3 meters, thinnest in unconsolidated soils and thickest in rock (Dallmann, 2015). Field investigation report by Wold (2015) indicates active layer thickness of 0.9 - 1.2 meters in Hotellneset. Study by L. Gilbert et al. (2019) shows active layer thickness of 1 meter in Adventdalen. In this area the top part of the ground consists of ice-rich epigenetic permafrost.

Thickness of the permafrost in Svalbard varies between 100m at the coast up to over 400m at the mountains (Dallmann, 2015; Harstad et al., 2018). Taliks might occur in vicinity of a water body or flowing water. Examples would be under a lake or pingos.

Ice-rich permafrost, such as found in Adventdalen, has a high water content meaning that the heat capacity of the medium is also higher. Thawing of ice will also require relatively high amount of latent energy. This means that thermal energy could be injected into the ground which is at the freezing point without increasing the temperature. This has a possibility of increasing the efficiency of BTES. On the other hand the efficiency can be decreased if the operating temperatures are above freezing point, in which case the ramp-up would consume unnecessary energy. Furthermore for this same reason, these areas take longer to react to the climate warming.

In some areas the temperature of the permafrost is close to thawing, especially in saline pore water environment where the freezing point depression causes PF to thaw already close to -2 °C (L. Gilbert et al., 2019). The zero annual amplitude - the level under which temperature fluctuations are not obserced - is typically at maximum 10 or 15 meter depth in soil and rock (Dallmann, 2015). However in suitable conditions the temperature fluctuations can be observed even deeper. Study by Harstad et al. (2018) shows temperature fluctuations as low as 15 to 20 m depth. The same study measured PF temperature to be -4.6°C at 15m depth in Janssonhaugen (circa 15 km inland into Adventdalen). However Geoscience Atlas of Svalbard (Dallmann, 2015) stated that the temperature at Janssonhaugen is -5.4 °C. There is three years of difference between the publication, but since the thermistor is installed in a deep borehole it might be more agile to record changes compared to natural ground, hence the lower recorded values. The same publication also provides PF temperatures of -6.0 °C in Adventdalen near the shore, and -3.0 °C at Kapp Linne. L. Gilbert et al. (2019) establish zero annual amplitude at 8 meters depth in Advendtalen, and at 9 meters depth in UNIS EAST. The corresponding temperatures are -4.0 °C and -3.6 to -3.7 °C. The general consensus is that permafrost temperatures are increasing globally, as stated by L. Gilbert et al. (2019).

Ground Thermal Regime

Ground temperature is affected by numerous factors including solar radiation, albedo, air temperature, precipitation, evapotranspiration and the thermal-physcial properties of ground material such as thermal diffusivity, heat capacity, density, water content and groundwater flow. Due to large number of parameters affecting the ground temperature, the simulation and modelling is complex and time consuming. A reliable and fast method is to measure the in-situ temperature for example from a borehole.

One of the first ground temperature measurements from deep boreholes in Svalbard were

performed in the 1990s by Isaksen et al. (2000). The measurements were made from 102 m deep borehole in Janssonhaugen (78°10'45"N 16°28'15"E 275 m.a.s.l.) circa 20 km east from Longyearbyen. The temperature gradient had a range of 2.5 - 3.7 $°C/100m$. Geothermal heat flux was estimated to be 67 mW/m^2.

According to measurements and simulations by Wawrzyniak et al. (2016) the temperature gradient near Hornsund is 3 $°C/100m$. The study estimated heat flux to be 44 - 70 mW/m^2.

Borehole logging by NGU shows temperature gradients from 20 meter interval ranging between 1 - 5 $°C/100m$ and 1 - 4.5 $°C/100m$ in boreholes Dh1 and Dh2 respectively (Elvebakk, 2008). For a 100 meter interval the results are 2 - 4 and 1 - 4 $°C/100m$. The boreholes are located near the shoreline by the road leading to Svalbard airport. Borehole Dh4, which is located in Adventdalen, was logged as a part of the same project. The temperature gradient measured from this borehole was 3.8 - 5.0 $°C/100m$ for a 100 meter interval(Braathen et al., 2012).

Research project run by Store Norske studied the feasibility of geothermal energy in Svalbard. The study concluded that the geothermal potential in the Svalbard is a lot higher compared to mainland Norway. Temperature models show geothermal heat flux of over 70 mW/m^2. The measured temperature gradient within the bedrock ranged mostly between 2 - 7 $°C/100m$. Modelled values indicated temperature gradient of 3 to 6 $°C/100m$. In both the modelling and observed data, values in the uppermost 200 meters were lower ranging from 0 - 2 (measured) and 0 - 5 (modelled) (Midttømme et al., 2015).

2.3 Climate

Svalbard is situated extremely north and lies between latitudes of 76°N to 81°N. However the climate is more moderate compared to other arctic areas, partly due to the North Atlantic drift also known as the "Gulf Stream" (Dallmann, 2015; Wawrzyniak et al., 2016). Svalbard experiences oceanic climate with relatively mild temperature fluctuations compared to other Arctic regions (Harstad et al., 2018). It is common for winter temperatures to drop close to -30°C, and summer temperatures rarely reach 10 to 15°C (Harstad et al., 2018). Mean annual temperature is -4°C (1979-2014) and the coldest month is March with -10.4°C mean temperature. (Wawrzyniak et al., 2016)

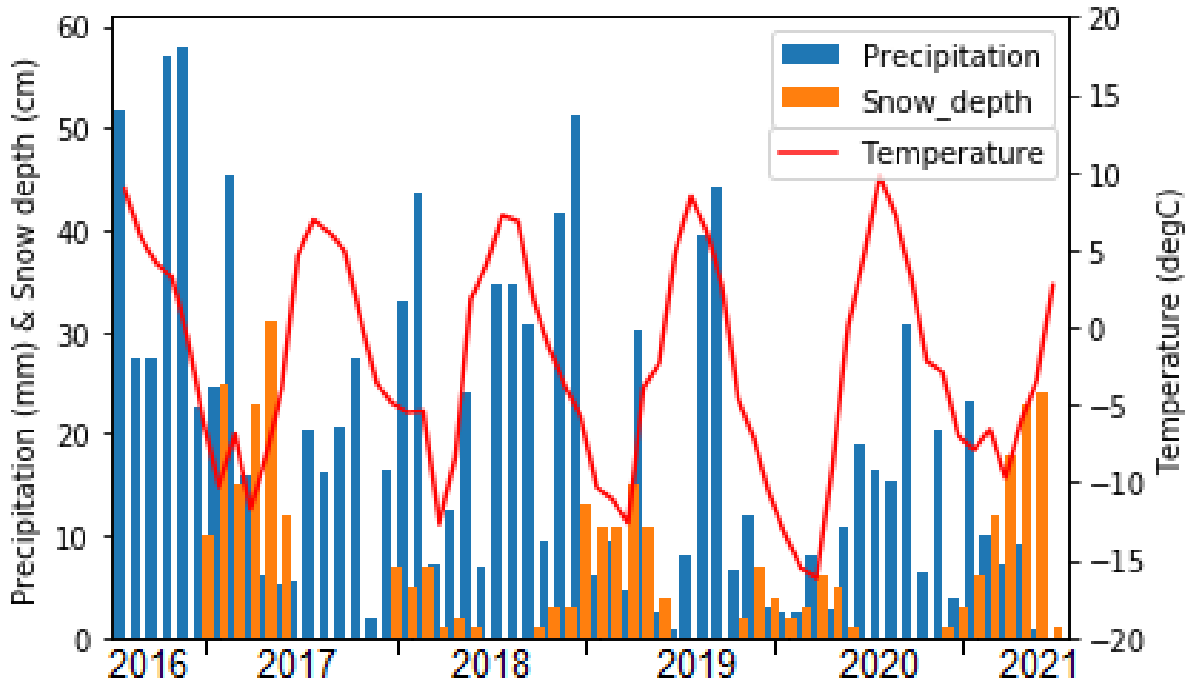

Figure 2.9: Average monthly air temperature, precipitation and snow depth data from Svalbard Airport from July 2016 to June 2021. Data from: The Norwegian Meteorological Institute (MET Norway) (2021).

Yearly precipitation is 453 mm at the Polish Polar Station in Hornsund (77°00' N, 15°33) (Wawrzyniak et al., 2016), 463 mm at the Isfjord radio (78°03'N 13°36'E) and 525 mm in Longyearbyen (78°13N 15°38'E) (Harstad et al., 2018). Much of the precipitation comes as a snowfall between October and June. Snowcover lasts 8 to 10 months, in Hornsund the snowcover lastes 238 days (1983–2014) and the mean snow cover is 17 cm.

Simulations show that annual precipitation can increase as much as 40% until the end of the century. Average temperature is forecasted to rise 4.0 to 5.3 °C (best to worst case scenario) until the mid 2000s and 3.6 to 9.2 °C at the end of this century. Highest rise is expected in winter temperatures: 5.7 to 13.4 °C. Summer 1.1 to 4.0 °C. Best case scenario shows that average temperature continues to rise for next decade, but stabilizes towards mid 2000s (Isaksen et al., 2017). Climate warming is observed in permafrost temperatures down to depth of 60 m (Wawrzyniak et al., 2016).

As a result of an extremely northern location, Svalbard experiences great yearly variation regarding sunlight and solar radiation. Longyearbyen experiences midnight sun from April to August and polar night (when the sun does not rise above the horizon) from October to February. (Time and Date AS, 2021)

Chapter 3

Borehole Thermal Energy Storage

Installed capacity of solar collectors and photovoltaics (PV) have steadily increased over the past years while the cost has decreased (Eisentraut and Brown, 2014). Solar energy production is highly intermittent, and for this reason energy storages are needed to fully utilize the potential of solar energy (Gao et al., 2015). As Welsch et al. (2016) states, seasonal energy storage is vital in correcting the mismatch between fluctuating energy demand and supply.

Energy can be found in many forms such as mechanical, electricity and heat and it can also be stored in various ways. Most common types of energy storages are electro-chemical e.g. batteries, potential e.g. pump-hydro, kinematic e.g. flywheel, and thermal storages. A categorized map of various energy storages can be seen in figure 3.1. Thermal storage can be further divided into sensible and latent thermal storages. In sensible heat storage, the energy is stored by increasing the temperature of the storage. Thermal Energy Storages (TES) can be further divided into Underground Thermal Energy Storages (UTES), or by operating temperature such as high-temperature or low-temperature TES. Examples of UTES are Aquifer Thermal Energy Storage (ATES), Pit Thermal Energy storage (PTES) or Borehole Thermal Energy Storage (BTES). (Lee, 2013; Dincer and Rosen, 2011)

3.1 Theory

Borehole Thermal Energy Storage (BTES) is a form of energy storage. Boreholes are drilled into the soil or bedrock, and heat is injected and/or extracted trough these boreholes. The most common method is to insert collector tube(s) into the borehole. Inside the collector there is a heat carrier fluid which has higher or lower temperature than the ambient ground medium, depending if heat is injected or extracted. Some systems have an open flow, where

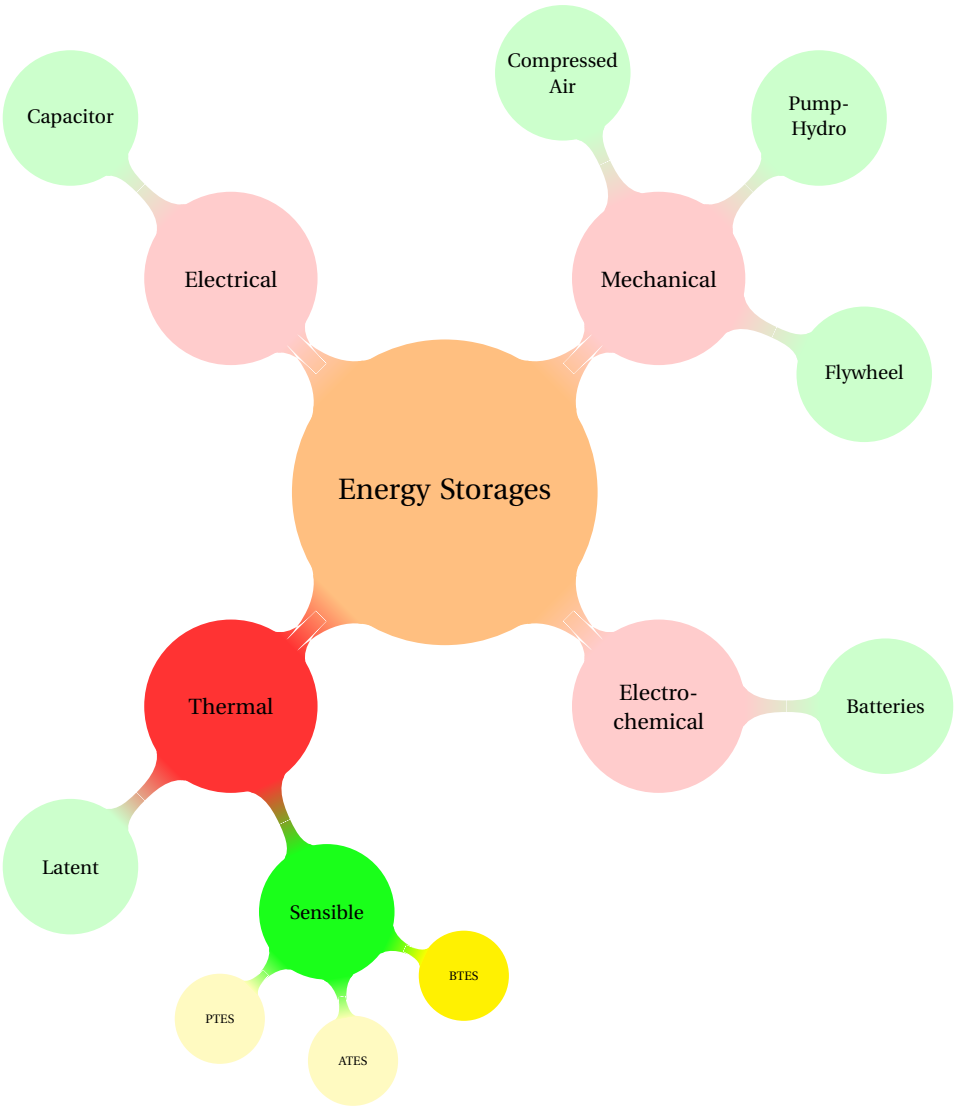

Figure 3.1: Various energy storage methods.

the heat carrier is directly in contact with the borehole wall. Heat transfer is based on a temperature difference. The Borehole is generally filled with a heat conducting material such as bentonite clay, grouts, concrete or quartz sand (Lee, 2013) but in some places the borehole is allowed to fill with groundwater. Figure 3.2 shows an illustration of BTES during loading and discharging phases.

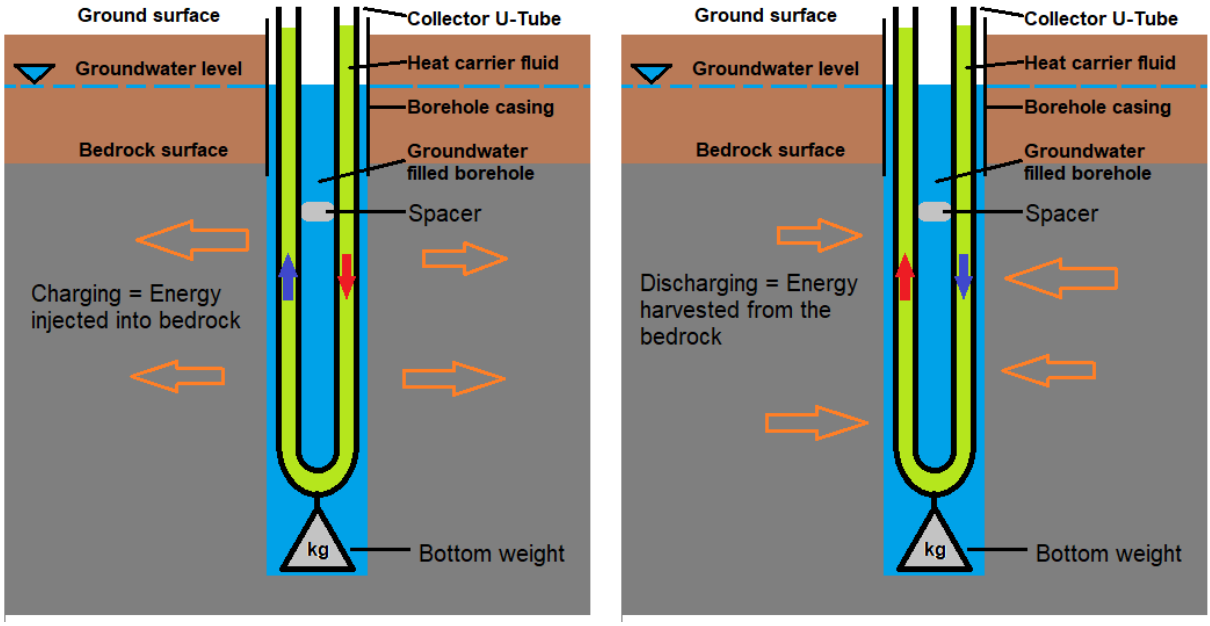

(a) Charging.

(b) Discharging.

Figure 3.2: Schematic of BTES with soil casing and a U-pipe collector.

BTES generally performs better as a long term (seasonal) storage and with a large capacity (Welsch et al., 2016). Other types of energy storages might be better suited for diurnal or peak shaving purposes. During the charging period, the BTES is "loaded" by circulating hot fluid inside the boreholes, from where the heat propagates radially deeper into the storage medium. During times of high energy demand and/or low production, such as during winter, this process is reversed. After the loading phase, the temperature of the storage has increased. During discharging period, cold fluid is circulated in the collectors embedded within the borehole. Now the heat flux is from the warmer borehole wall, into the colder heat carrier fluid. The energy will heat up the fluid, and this energy can be used for heating purposes.

The amount of energy stored per volume is directly proportional to the volumetric heat capacity and operating temperature of the BTES system. The higher the density and specific heat capacity of the medium, the smaller space is occupied to store certain amount of energy per temperatuer difference.

Contrary to a conventional geothermal heating system, groundwater flow is usually detrimental to the efficiency of the BTES. Flowing groundwater will transport the heat away from the storage by the means of convective heat transfer. This is why BTES systems will not perform optimally in highly permeable storage mediums. (Nielsen, 2003; Reuss, 2015; Giordano and Raymond, 2019)

The boreholes are generally drilled vertically into the ground. In some cases they might be intentionally made diagonal. One reason to deviate the boreholes could be limited surface area, which does not allow so many boreholes. Instead of drilling longer boreholes, they can be deviated to create larger storage volume. An example can be seen in figure 3.3d.

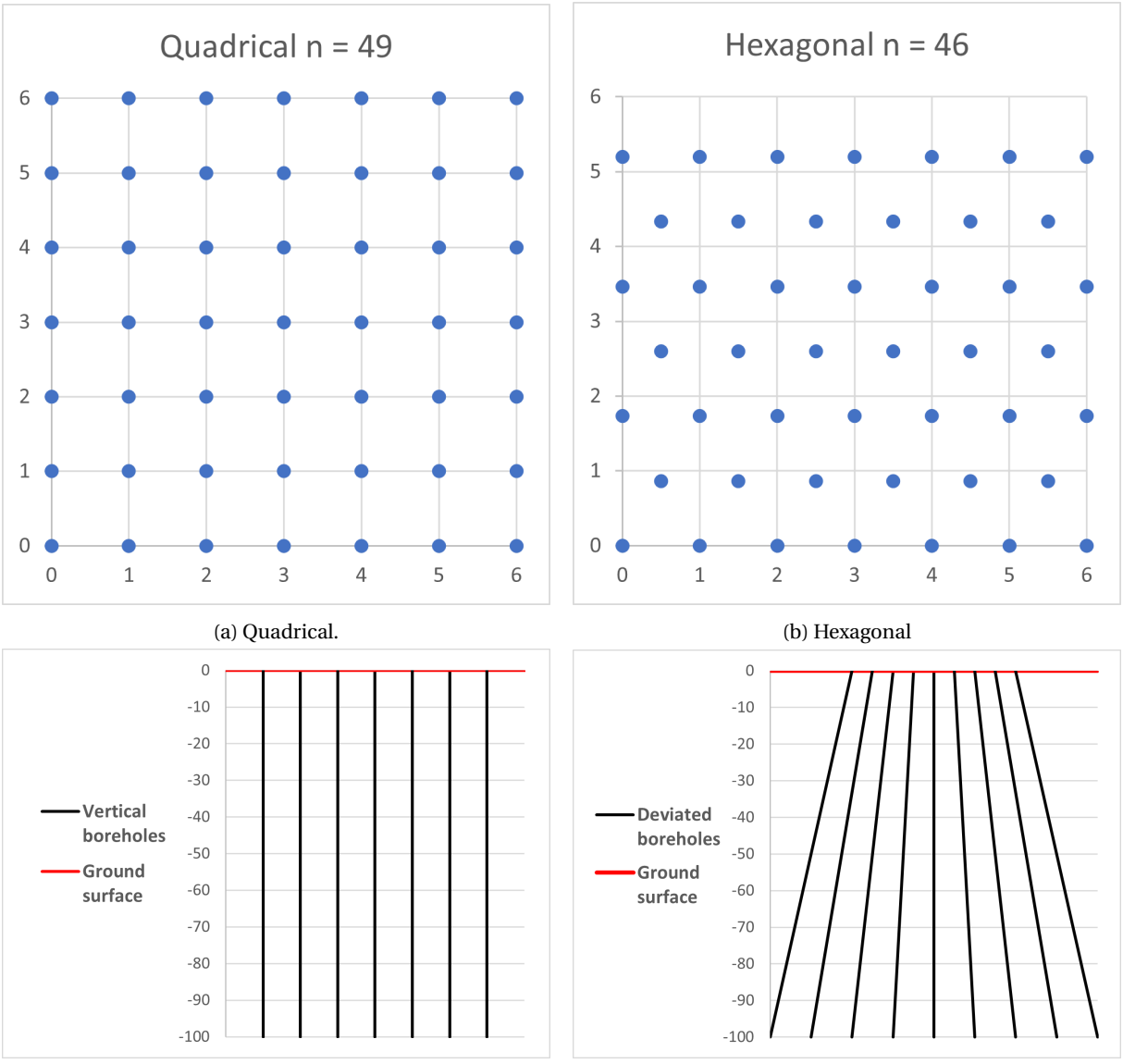

(a) Quadrical.

(b) Hexagonal

(c) Vertical

(d) Deviated

Figure 3.3: BTES patterns and borehole alignment

As seen in figures 3.3 the borehole field can be drilled into various patterns, quadrical and hexagonal being the most common types. Hexagonal pattern is more efficient because it decreases the perimeter - surface-area (in 2D) or surface-area - volume (in 3D) ratio. (Reuss, 2015; Johnsson, 2017). Examples of the area-perimeter ratio can bee seen in figure 3.4. Minimizing this ratio is important, because the capacity of the storage is dependant on the area, but heat losses depend on the perimeter.

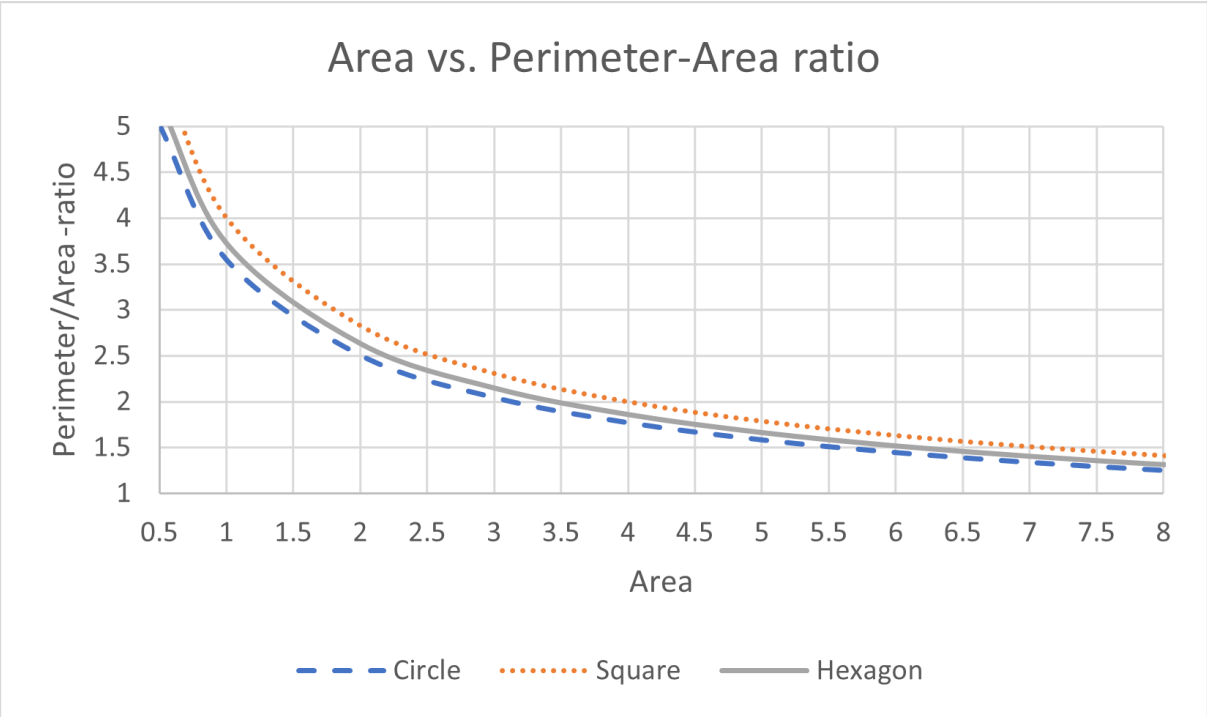

(a) Perimeter to area ratio with three different shape.

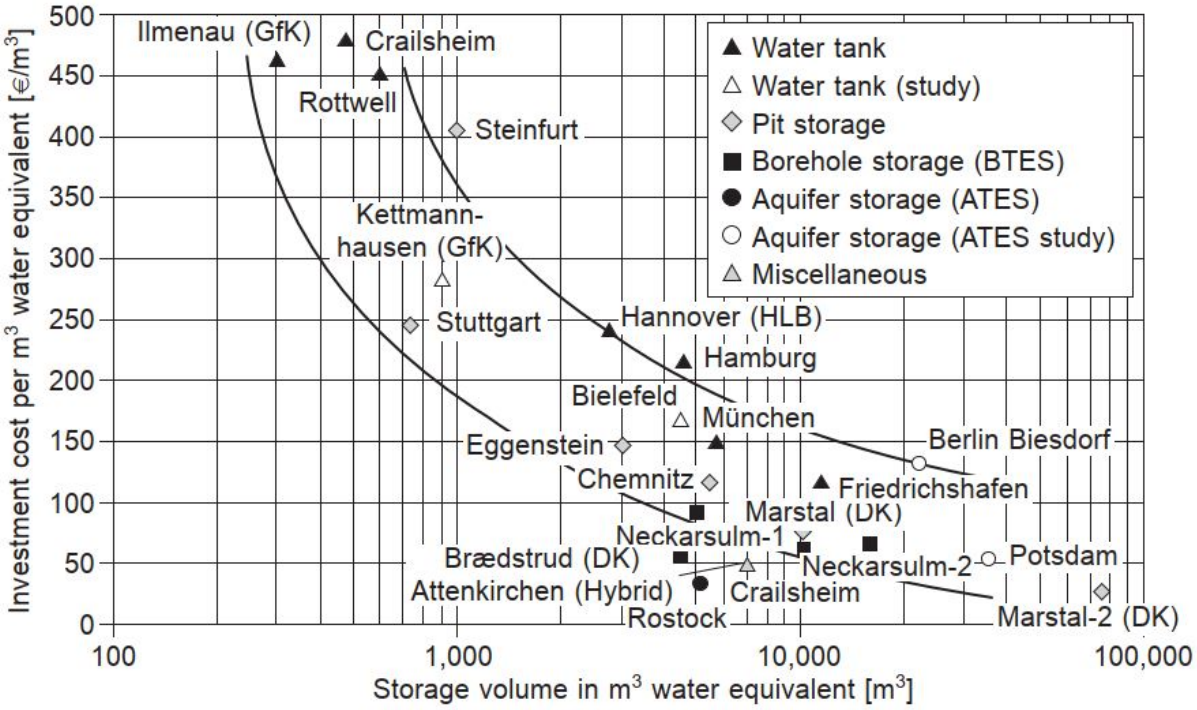

(b) BTES investment cost per storage capacity as a function of storage capacity. Figure edited by Reuss (2015), original graph from Mangold et al. (2012)

Figure 3.4: BTES perimeter to area ratios with various borehole drilling patterns and investment cost related to the size of the storage.

Boreholes can be connected in series or parallel (Sun et al., 2020). In parallel connection all of the boreholes receive approximately same amount of energy (same inlet temperature and flow rate) or in other words the input energy rate is not affected by the energy transfer in

other boreholes. Other method is to connect boreholes in series, so that the heat carrier fluid travels trough one borehole, after it goes trough one or more boreholes. An example of this was done in Drake Landing Solar Community in Okotoks, Canada with 24 parallel strings, each with 6 boreholes in series (Reuss, 2015). This allows to create a temperature distribution into the storage. Common method is to start injecting/extracting of the energy from the middle of the storage, and move outwards. This will cause stratification with hot temperature in the middle and colder temperatures near the periphery. This has been shown to increase the efficiency and decrease heat loss in the system. Dai et al. (2015) observed increased COP with boreholes connected in series compared to parallel.

3.2 Components

Acuña (2013) divides borehole heat exchanger into following components:

- Borehole wall and surrounding ground

  Typical borehole diameter is up to 150 mm. In good quality bedrock the borehole can be drilled easily. In poor quality bedrock or sedimentary soils, borehole needs to be lined with casing to prevent collapse. Even in good quality bedrock, the borehole walls are not 100% intact, but instead there are small cracks and fissures.

- Collector

  Collectors are made in various types, and from various materials. The most common types are Coaxial or U-Pipe.

  The shape of a U-tube or U-pipe resembles the letter 'u', hence the name. Inlet fluid flows downwards from one branch, and outflow is upwards in the other branch. Sometimes multiple U-Tubes can be installed into the same borehole to increase efficiency and reliability. Even if one tube gets clogged the other one still operates. Spacers for U-tubes are recommended to reduce short-circuiting of heat, i.e. heat transfer directly between the inlet and outlet pipes. U-tubes are more reliable, easier to install and cheaper compared to coaxial pipes. (Reuss, 2015; Gehlin, 2016)

  Coaxial or pipe-in-pipe system consists of two pipes where the smaller diameter pipe is within the larger pipe. In coaxials the inflow can happen either from the outside or inside pipe. In BTES system the inflow is most commonly in the outer pipe.

  Materials are usually polymers, or in some cases metal. Plastic pipes are most common

since they do not corrode, are flexible and cheap. Metal has better heat conductivity and can withstand high temperature and pressure. (Reuss, 2015). The inner surface of the pipe might have been engineered to produce turbulent flow, since turbulent flow has better heat transfer properties compared to laminar flow.

- Heat carrier fluid

  Water has good thermal properties to be used as heat carrier in the BTES system when it is constantly operated above +4C. However using regular water has drawbacks because of the freezing point, which might be above the ground temperature. For this reason antifreeze agents such as ethanol, propylene or ethylene glycol are often mixed into the fluid. Ethanol is however unsuitable to be used in high temperatures. (Gehlin, 2016)

- Grout/fill

  Empty space left in boreholes after installation of the collector is filled to ensure proper thermal contact between the collector and the borehole wall. Filling can be done with regular ground materials, but most common method is to fill it with specially engineered grouts with high thermal conductivity (Reuss, 2015). However in many scandinavian countries the boreholes are allowed to naturally fill up with groundwater. (Gehlin, 2016)

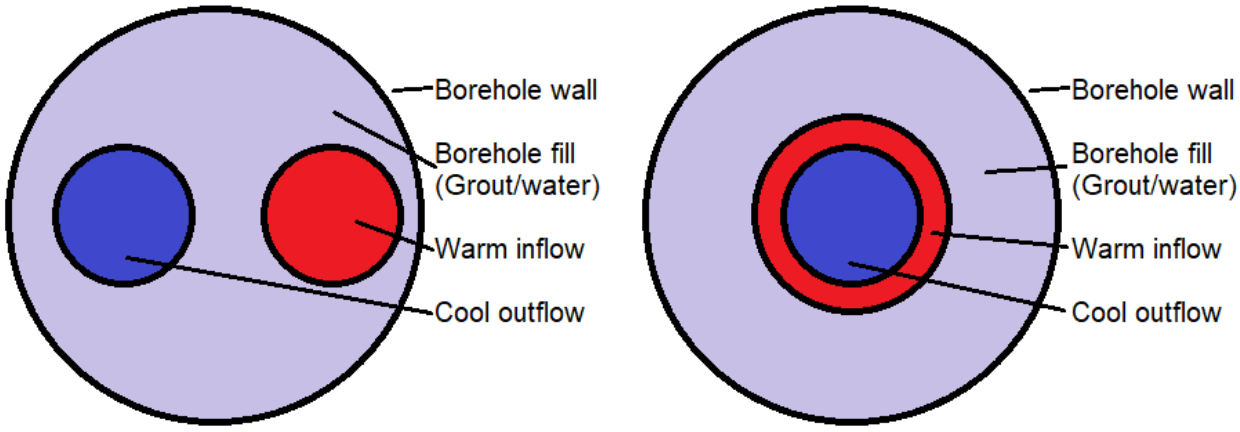

(a) U-Pipe (b) Coaxial

Figure 3.5: Top view of a cross-section of the U-Tube and coaxial pipe within a borehole.

Additional components related to the system might also include external components such as heat pump(s), buffer tank for short term energy storage, monitor and control units, distribution network and so on.

3.3 Examples

Table 3.1 shows information of seven BTES systems from Canada, Norway, Sweden and China.

Table 3.1: Physical and thermal parameters of the carrier fluid 50%-vol Kilfrost GEO / water.

Location	**Boreholes (n and depth)**	**Storage medium**	**Reference**
Oshawa, Ontario, Canada	374 x 200m	Limestone, Shale	Dincer and Rosen (2011)
Akershus, Oslo, Norway	228 x 200m	Mostly bedrock	Bäcklund (2009)
Emmaboda, Sweden	140 x 150m	Granodiorite	Nordell et al. (2015)
Tianjin, China	3789 x 120m	Soil	Yin and Wu (2018)
Stockholm, Sweden	144 x 200m	Mostly bedrock	Skanska AB (2014)
Grosvad, Fingspång, Sweden	126 x 110m	-	Edstedt and Nordell (1994)
Kuujjuaq, Nunavik, Canada*	100 x 30m	Soil	Giordano and Raymond (2019)

*Simulated BTES with ground properties determined by in-situ and laboratory tests.

Table 3.1 shows that BTES are operational all over the world, in different sizes and different ground mediums. The most relevant case regarding this study is the one in Kuujjuaq, Canada. Kuujjuaq(58°N 68°W) is the largest town located in Nunavik, northern part of the Quebec province of Canada. Kuujjuaq lies in subarctic climate zone with an average annual air temperature of -5.8°C. According to Allard and Lemay (2012) the town is located within discontinuous permafrost. However field investigations at the proposed BTES site concluded that the ground is unfrozen, most likely because of the talik surrounding the nearby lake. Giordano and Raymond (2019) simulated a BTES system in the area. The results concluded that the high subarctic environment is not an obstacle for a BTES.

3.4 Limitations and Risks

While BTES is extremely versatile technology, and can be used in almost any geological conditions it still faces some limitations (Lee, 2013). Like with most infrastructure, available space is an issue. BTES has advantages that it can be constructed even on a small area, and under existing or planned constructions. The technical facilities needed for operation can be embedded into technical rooms of the superstructures. The main concern with the BTES is collision with possible existing underground structures especially in urban areas. For this reason many cities have enforced underground zoning plans.

BTES might be not allowed to be built in aquifer areas. Even if the site would otherwise be ideal, if the area is used as aquifer for drinking water BTES might not get permitted. Even

if only water is used as heat carrier fluid, eliminating the possibility of a toxic spill from antifreeze additives, the temperature change in the aquifer caused by the BTES might cause contamination.

Operational challenges arise from the quality of BTES materials. For example plastic collector pipes do not tolerate high temperature. Metal pipes would be a solution, but the problem with metal is corrosion. Many metals corrode easily in saline environment of for example in areas with sulfide clays.

Environmental risks associated with BTES are mainly related to the heat carrier fluid, which might be toxic. Possible hazards include potential groundwater pollution in the case of spill. In some countries the legislation forces that boreholes have to be grouted to limit the spread of possible contamination.

Possible risk is also puncturing holes between different layers of groundwater. This would cause mixing of different aquifers. In some instances the cap of pressurised artesian water body could be penetrated causing outflow of water. In addition to flow of water at the drill site, the groundwater level on other connected areas might lower, causing risk of settlements and even damage to structures.

Chapter 4

Field Work

Fieldwork was conducted during March and April in Longyearbyen, Svalbard. The test sites were predetermined by the local government; one site on bedrock with a thin topsoil, other on a marine deposit. Locations can be seen in figure 2.6 in section 2.2. The fieldwork chapter is divided into three sections: 1. Drilling, 2. Sampling and 3. TRT test.

Test site

The two test sites were chosen by the local government. Sites are named numerically in a chronological order. Site 1 was drilled first and Site 2 second. These sites could later be used as a part of the future BTES, if one is chosen to be built. Site 1 is promising due to multiple reasons. 1) The soil layer at the site is thin, meaning that solid bedrock is easily accessed. 2) The area is prone to avalanches. This might sound counter-intuitive, but it means that no residential or commercial buildings will be constructed there - thus the site does not compete from the constructable area in the town. Site 2 is located on the coastal lowland between airport and coal harbor.

4.1 Drilling & Installing the Collector Tube

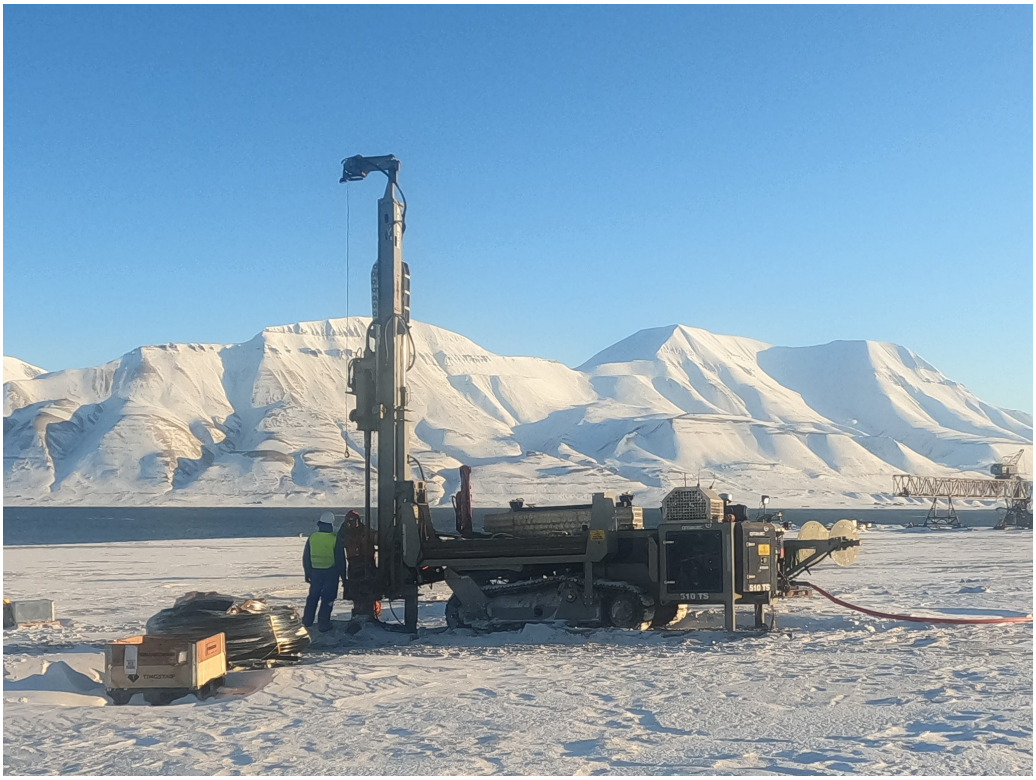

Figure 4.1: Drilling at the drillsite 2.

4.1.1 Methodology

The drilling was done with a remotely controlled, track based drill rig. Flushing was done with air to 1) minimize permafrost thaw and 2) to eliminate clogging of the borehole from freezing water during pauses in the drilling. Drilling method was Down The Hole (DTH), which means that the hammering is done down in the hole instead of on top of the drill rods. Casing was used in the soil layers to prevent the borehole from collapsing. The soil casings were connected to each other by welding. Drill rods had threads so they could simply be connected by screwing them into each other. Each drill rod and casing was 3 meters long, so drilling had to be paused every 3 meter to extend the rod. The borehole diameter with the casing was approximately 150 mm and without the casing 115 mm. Part of the drilling process related to extending the soil casing can be seen in figure 4.2.

(a) Heating.

(b) Welding.

Figure 4.2: Heating and welding for extending of a soil casing.

Grout or any special fill material was not used for this project. The borehole was allowed to fill with groundwater. To prevent the borehole from freezing, salt was added into the water. 2.5 m^3 of water at 55°C was mixed together with 78 kg of salt. Approximately 1 m^3 of brine, now at 30-35°C was stepwise trickled into the borehole.

After the borehole was drilled it was time to install the collector. This was only done at the site 1 because sufficient depth was not reached at the drill site 2. Heat transfer fluid was already within the collector. The collector was delivered on a coil, from where it was lowered into the borehole. Weight was inserted into the lower end of the colletor to ensure that the collector would reach the bottom of the borehole. This was done because saline water is more buoyant than fresh water. Due to the high length and weight of the collector system, special device was mounted on top of the borehole to ease the process (see figure 4.3). This device has an electrical engine which can either help to push the collector downwards, or brake the collector if it would start to plummet into the borehole too fast.

(a) Collector before uncoiling.

(b) Installing of the collector tube.

Figure 4.3: U-pipe collector.

Temperature measurements were logged also along the length of the whole borehole. For this reason two optical fibre cables were inserted; one into the downflow, and the other one to the upflow pipe.

4.1.2 Results & Observations

The drilling process itself provided valuable information about the subsurface. At site 1 the first observation was "blowout" of water at approximately 9 to 12 meters depth. Since the ground was frozen and air was used as a flushing medium, hypothesis is that groundwater flows within this layer. The drill site is located near a mountain slope, so this water flows probably from the mountains. There is also a small meltwater river running adjacent to the site. Topsoil was approximately 9 meters thick. Soil casing was extended into 12 meters depth.

Extent of permafrost was easily recognized from the drilling. Since flushing was performed with compressed air, the drill cuttings were totally dry, dust-like, material. Below permafrost the natural liquid water within the bedrock caused the drill cuttings to be wet and appear more muddy. This is shown in figure 4.4. The change from dry to wet was first observed when the drill bit was at 150 meters depth, thus the permafrost is assumed to extend until this depth at this location.

(a) Dry cuttings while drilling in permafrost.

(b) Wet cuttings while drilling in thawed environment.

Figure 4.4: Difference between dry and wet drill cuttings while drilling in and beneath the permafrost.

The drilling rate was relatively constant throughout the drilling. The drilling time for 3 meters length ranged from 2 to 9 minutes, but mostly stayed between 3 to 4 min. This can be seen in the figure 4.5. From this data the hypothesis is that the bedrock is relatively homogeneous regarding the mechanical properties. According to the drill operator the advance rate was good.

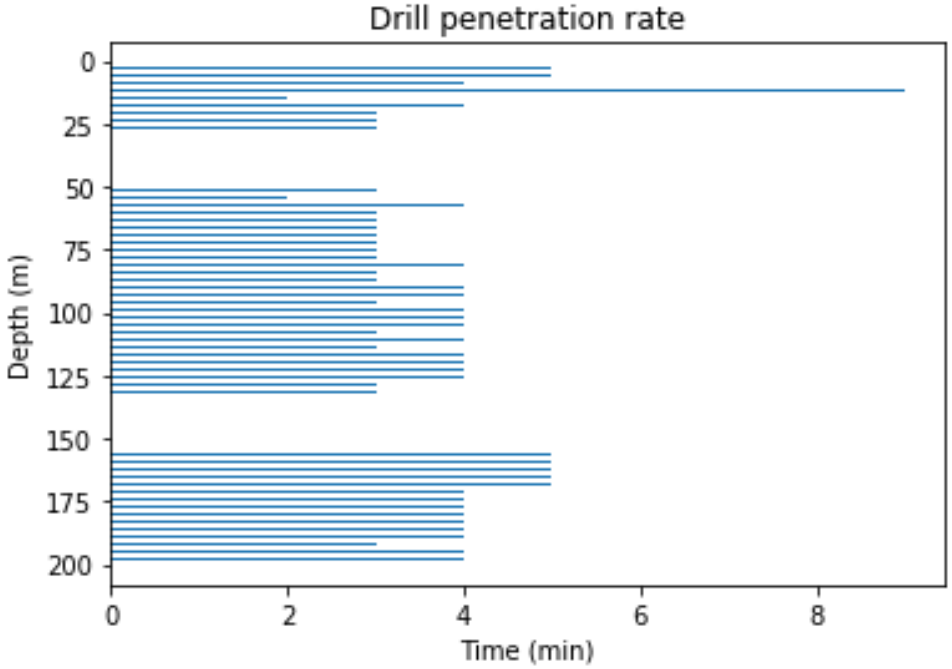

Figure 4.5: Drilling time as a function of depth.

After the drilling it was observed that the groundwater in the borehole was bubbling. This was thought to be pressurised air from the flushing, escaping the small fissures in the bedrock. However this continued over the next day, which raised questions about the source of this gas. Scientists from the geology department at UNIS arrived at the site and analyzed the gas to be methane. Precautions were made due to possibly hazardous gas. Also the installation could not be fully finished until the methane seepage stopped, because plugging the borehole during gas buildup could have risked pressure explosion within the borehole.

4.1.3 Limitations

Extending the soil casing took relatively long time. Welding together new piece of casing took close to 15 minutes where as a new drill rod could be placed within a minute. For this reason drilling in soil layers is a lot more slower than drilling in intact bedrock due to the soil casing. This could be eliminated by having soil casing with threads, but that would increase the price of the components. Drilling at the site no. 2 required co-operation with the airport operator. Airport had to be informed before the drilling, since there are equipment which are sensitive to vibrations. This was not an issue during the drilling of one borehole for the TRT, but if full scale BTES (hundreds of boreholes) would to be constructed in the area this would have to be taken into consideration when planning drill schedules.

Another limitation is related to the isolation and remoteness of the Svalbard archipelago. The 2nd borehole was also planned to extend down to 200 meter depth. However since all the soil casings were used, and bedrock was still to be reached the drilling could not be continued. In areas with comprehensive traffic infrastructure, this problem could have most likely solved by ordering more casing tubes to the site. These could have been brought to the site by the next day and drilling could have continued. However this is typical logistical issue arising when operating in Svalbard. Only methods of transportation are by boat or a plane. Also due to small economy, there are no stockpiles for many items.

4.2 Sampling

Samples were taken from the drill cuttings for later use. The sampling process was extremely rough and the sample depths are to be considered indicative.

4.2.1 Methodology

Drilling of the borehole produces drill cuttings with a diameter of generally less than few centimeters. These drill cuttings were collected into a bucket and a shovel was used to transfer few hundred grams to few kilograms of samples into a sampling bag. Samples were collected in a three meter depth intervals. Bucket was emptied every three meters, when a new drill rod was added.

(a) Setup for sampling.

(b) Sampling process.

(c) Results of sampling.

(d) All samples. Colour difference between some of the samples can be seen from the picture.

Figure 4.6: Sampling process and all samples colleted together.

Estimation of Thermal Conductivity Based on Mineralogy

Various models are created to estimate the thermal conductivity of ground materials using mineralogical content. Côté and Konrad (2005b) used geometric mean method shown in equation 4.1 to calculate thermal conductivity of solid particles. Calculated values correlated well with measured values and data from literature.

$$k_s = \prod_{j=1}^{z} k_{mj}^{x_j} \quad \text{with} \quad \sum_{j=1}^{z} x_j = 1 \tag{4.1}$$

where:

k_s = thermal conductivity [$\frac{W}{m*K}$]

z = total number of minerals [-]

j = j^{th} mineral [-]

k_m = thermal conductivity of the mineral [$\frac{W}{m*K}$]

x = volumetric proportion of mineral [-]

In a fully saturated ground, Johansen (1975) proposes a geometric model shown in 4.2.

$$\begin{aligned} k_{sat(u)} &= k_s^{1-n} k_w^n \quad T \geq 0°C \\ k_{sat(f)} &= k_s^{1-n} k_i^n \quad T < 0°C \end{aligned} \tag{4.2}$$

where:

k_s = thermal conductivity solid [$\frac{W}{m*K}$]

k_w = thermal conductivity of water [$\frac{W}{m*K}$]

k_i = thermal conductivity of ice [$\frac{W}{m*K}$]

$sat(u)$ = saturated unfrozen [-]

$sat(u)$ = saturated frozen [-]

n = porosity mineral [-]

There are various other methods to calculate thermal conductivity based on mineral content. However in this work the mineralogy based estimate was calculated using the equations above. Since the composition of the amorphous content is unknown, this is given value of 2 $\frac{W}{m*K}$.

4.2.2 Results

The samples were visually inspected. Colour, grain size and water content was logged. This qualitative assessment was done by sensory observation, so the results are not absolute. The samples were compared to each other and the results were noted down on a spreadsheet. Total of 15 samples were sent for X-Ray Diffraction (XRD) to determine the mineralogical content. The mineralogy based on the XRD can be seen in figure 4.7.

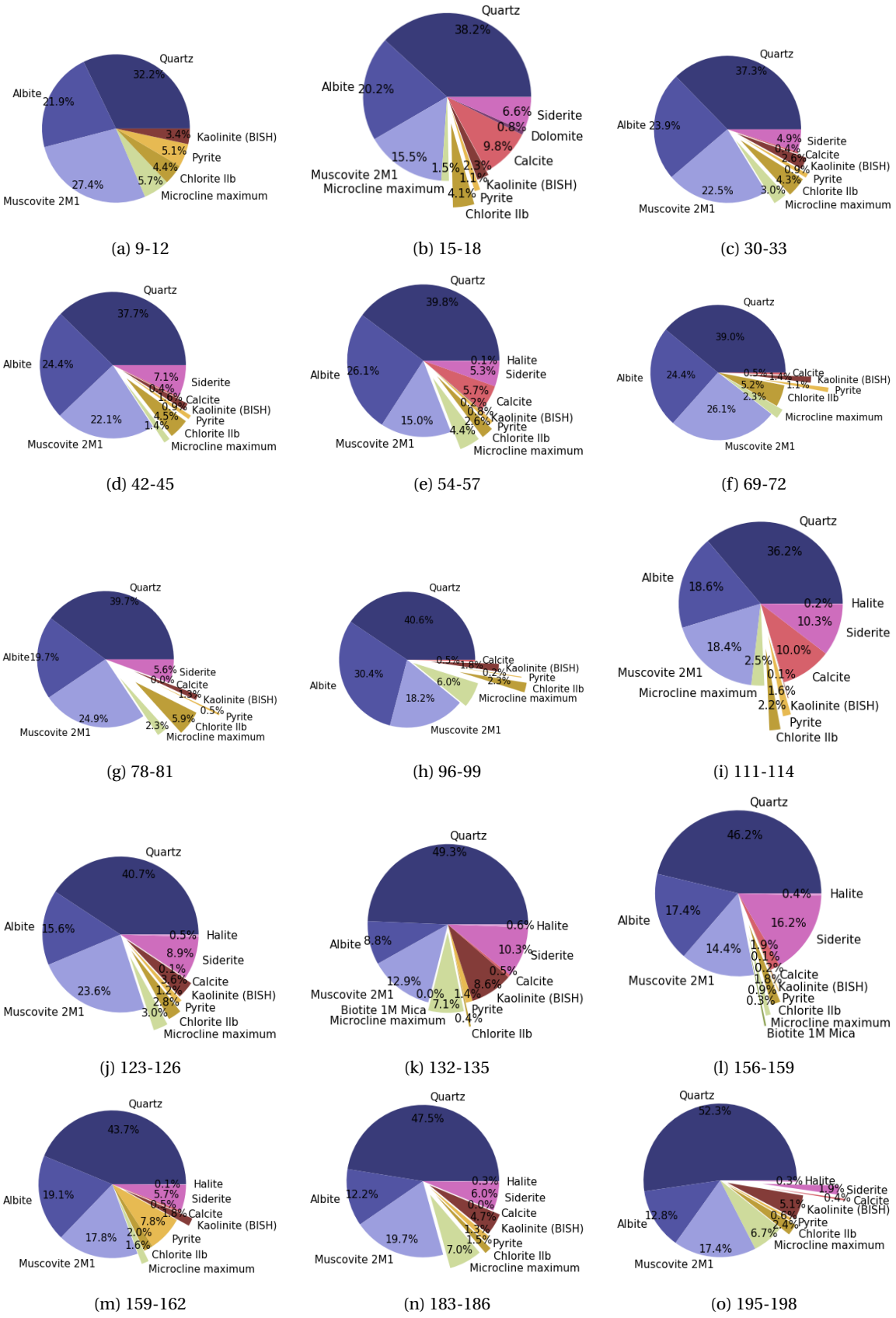

(a) 9-12 (b) 15-18 (c) 30-33

(d) 42-45 (e) 54-57 (f) 69-72

(g) 78-81 (h) 96-99 (i) 111-114

(j) 123-126 (k) 132-135 (l) 156-159

(m) 159-162 (n) 183-186 (o) 195-198

Figure 4.7: Mineral content of crystalline material from 15 samples determined by XRD.

As seen from the figure 4.7, the quartz content throughout the borehole varies between 32

and 52 %. Quartz is a mineral with high thermal conductivity of 7.69 $\frac{W}{m*K}$ according to Côté and Konrad (2005b). High thermal conductivity promotes fast heat transfer in the bedrock, making quartz bearing bedrock well suited as a medium for BTES and other geothermal heating or cooling systems.

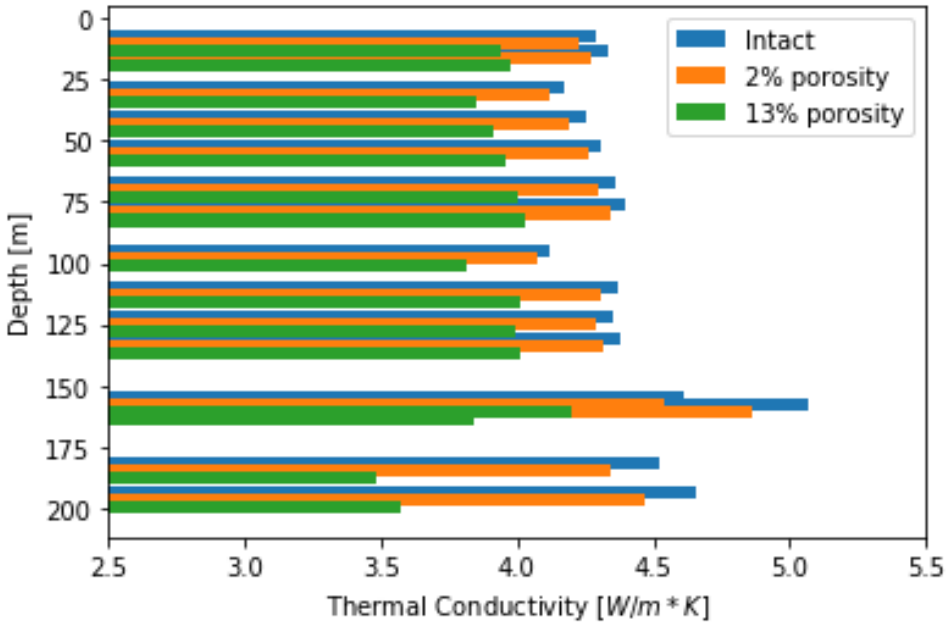

(a) Mineralogy based on crystalline material.

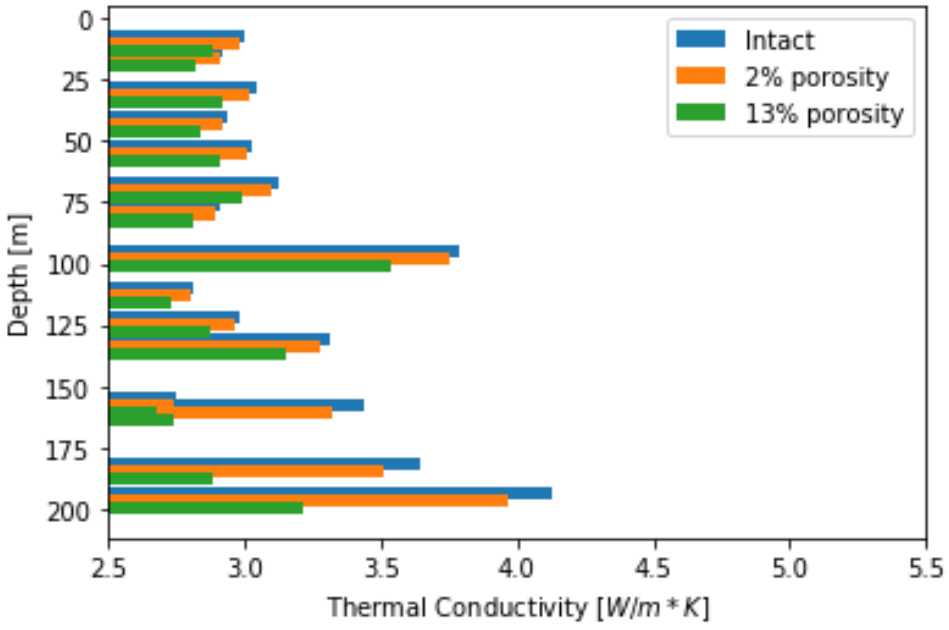

(b) Mineralogy including the amorphous material.

Figure 4.8: Thermal Conductivity Estimated by Mineralogy Based on Crystalline Material and Amorphous Content.

As seen in figure 4.8a, thermal conductivity calculated purely based on the mineralogy from XRD shows little variance in the values along the length of the borehole. Only in after

150 m depth a noticeable spike is shown. Thermal conductivity calculated taking amorphous content also into account, shown in figure 4.8b, shows spikes at 100 and 200 meters depth. In both graphs shown in figure 4.8 the difference between intact rock and 13 % porosity increases dramatically after 150 meters depth. This happens because the thermal conductivity is calculated in frozen state above 150 m and in unfrozen state deeper than 150 m, and since ice has over 3 times higher thermal conductivity than water.

4.2.3 Limitations

The depth from where the samples were retrieved is indicative. It is assumed to be mostly from the 3 meters distance, but in reality each sample can contain traces from rock along the whole borehole length drilled so far.

Also the amount of drill cuttings per each 3 meters of borehole was too much to be collected into the bucket nor sample. Each sample represents approximately 1-2 % of that specific population. Due to the sampling method segregation of drill cuttings occurred, and the fraction that was sampled was highly dependant on the distance of the bucket from the cutting outlet, flushing fluid pressure and prevailing wind conditions. This means that samples could show larger difference in the content than what is the real situation within the whole population.

XRD only shows mineral content of the crystalline material. According to the XRD report amorphous content was 29 to 55 % of the tested materials. For this reason the exact mineral composition is unknown.

4.3 TRT

The performance of geothermal systems such as ground heat exchangers are based on thermal properties of the ground medium. These properties include thermal conductivity, capacity and diffusivity. In smaller projects such as single-family house these are generally estimated from literature or from knowledge gained from previous projects, however in larger systems precise estimation is extremely important. The properties should be measured on site to optimize dimensioning of the system such as amount and length of the boreholes. Limited knowledge of the in-situ properties might result in over or underdimensioning and poor operation and economics of the project. (Witte et al., 2002; Sanner et al., 2005; Jensen-Page et al., 2019; Franco and Conti, 2020; Raymond et al., 2011; Marcotte and Pasquier, 2008; Borinaga-Treviño et al., 2013)

Figure 4.9: TRT rig at drill site 1.

Proven method for in-situ testing of ground thermal properties is the Thermal Response Test (TRT). Traditional TRT provides efficient thermal conductivity over the length of the whole borehole and the borehole thermal resistance. It takes into consideration possible thermal convection caused by groundwater flow. Literature values are the fastest and easiest to obtain, but due to variance in regional and local ground conditions the range of values is high. This makes it hard to find and select proper values. Laboratory testing is a valid option, but this requires facilities and equipment to perform the tests. In lab testing there is always possibility of sample disturbance and contamination. Regarding thermal conductivity one sensitive parameter is the water content. Also the results from laboratory tests can not take into consideration possible groundwater flow on the site. (Witte et al., 2002)

4.3.1 Theory

First ideas of TRTs took place in the 1980s and 90s (Hakala et al., 2014). First TRT apparatuses were built in Luleå, Sweden in 1995 and independently in Oklahoma State University

in Austin, USA in 1996. These were based on constant heating of the heat carrier fluid, where as a heat-pump based system was developed in the Netherlands. This Dutch version, discussed by Witte et al. (2002), in addition to heating the ground, it was also able to extract heat from the ground. (Sanner et al., 2005)

Raymond et al. (2010) measured in-situ thermal conductivity utilizing heating cables instead of conventional closed-loop liquid circulation. The paper concluded that heating cables have advantages over traditional method, such as the test system is much more compact, it can be fully automatized and the line-source-method is better applied since the heating is located within the borehole and is not as sensitive to temperature variations on top and near the ground surface. Other advanced TRT systems include Distributed Thermal Response Test (DTRT),Thermal Response Test While Drilling (TRTWD), enhanced Thermal Response Test (eTRT), Constant Heating Temperature Method (CHTM) and Thermal Cone Dissipation Test (TCT) (Franco and Conti, 2020). Some of these, such as TRTWD and TCT can be combined to other geotechnical investigation methods, allowing them to be performed simultaneously. Since field investigations are conducted in almost every construction project, combining these with TRT tests could provide synergy benefits in a from of time and cost savings.

DTRT uses Distributed Thermal Sensing (DTS) to record temperatures along the borehole length. This is done by installing fiber optic cables into the collector tube. Unlike the conventional TRT which provides “average” thermal conductivity for the whole borehole, DTRT shows the vertical distribution of thermal conductivity aswell as the borehole thermal resistance. (Hakala et al., 2014; Acuña, 2013)

DTS is widely used in different industries to record real time temperature data along a long distance. It can be used to measure temperatures in pipelines, power cables, oil wells and also as a fire detection in tunnels and tall buildings. Even if the cable is damaged in a certain point, it can still provide data up to the breakage point. DTS can measure thousands of data points simultaenously, and the spatial resolution is typically tens of centimeters. DTS measurements are based on sending a laser pulse in an optical fibre glass. Most of the light passes trough without change, but some is deflected and some refracted. This scattered light is mostly Raman, Rayleigh and Brillouin scattering. The wavelength of reflected anti-stokes scattering is temperature dependant. In other words temperature of the fiber optic material (typically quartz glass) changes the molecular lattice, which causes differing properties to the reflected light. Since the time when the laser pulse has been sent, and the speed of the

pulse within the cable is the speed of light, the distance of travelled light can be easily calculated. The distance to the scattering point is essentially half of the distance that the light has travelled, providing spatial data of the measurement. Spatial resolution is mainly dependant on how accurately time can be recorded. (Hakala et al., 2014; Acuña, 2013)

Thermal conductivity

The basic principle of TRT is to excite a heat transfer between the borehole and the surrounding medium. This is done by either heating or cooling the surrounding ground, and then monitoring the response. In practice this is done so that fluid is circulated in the borehole. The inlet and outlet temperature aswell as the flow rate are measured. There are multiple methods to analyse the response, line source method (LSM) being one of the most common. LSM is also used in this work. The average fluid temperature between the inlet and outlet is plotted against time in logarithmic scale. The k value represents the slope of the curve. The value of the effective thermal conductivity can then be calculated with the equation 4.3.

$$\lambda = \frac{Q}{4\pi h k} \tag{4.3}$$

where:

λ = thermal conductivity $[\frac{W}{m*k}]$

Q = energy [W]

h = efficient (grout/water filled section) depth of borehole [m]

k = slope [-]

$$Q = c\dot{m}\Delta T \tag{4.4}$$

where:

c = specific heat capacity $[\frac{J}{kg*K}]$

$\dot{m}$ = mass flow $[\frac{kg}{s}]$

ΔT = temperature difference $(T_{in} - T_{out})$ [K].

Borehole Thermal Resistance

The borehole thermal resistance can be calculated with equation 4.5. This is an empirical method based on the measurements from TRT.

$$T_f - T_{bw} = R_b * q \tag{4.5}$$

where:

T_f = Average temperature of the heat carrier fluid [K]

T_{bw} = Temperature of the borehole wall [K]

R_b = Borehole thermal resistance [$\frac{K}{W}$]

q = Energy transfer rate [W].

There are also theoretical methods to estimate the borehole thermal resistance. The thermal resistance between the heat carrier fluid and the borehole wall consists of three components, 1) resistance between the fluid and pipe wall (see Equation 4.6), 2) resistance through the pipe wall (see Equation 4.11) and 3) resistance trough the grout/fill material in the borehole (Equation 4.12 and Equation 4.13). All the relevant equations and explanations are shown below and are from the paper by Hakala et al. (2014).

$$R_f = \frac{1}{2\pi r_i h} \tag{4.6}$$

where:

R_f = Thermal resistance between the fluid and inner pipe surface [$\frac{K*m}{W}$]

R_i = Inner radius of the collector pipe

h = Convective heat transfer coefficient

$$h = \frac{\lambda_f}{D} * Nu \tag{4.7}$$

where:

λ_f = Thermal conductivity of the fluid [$\frac{W}{m*K}$]

D = Inner diameter of the collector pipe [m]

Nu = Nusselt number [$-$]

$$Nu = \frac{(\frac{f}{8})(Re-1000)Pr}{1+12.7(\frac{f}{8})^{0.5}(Pr^{\frac{2}{3}}-1)} \tag{4.8}$$

where:

f = Friction factor $[0.79ln(Re)-1.64]^{-2}$

Re = Reynolds number [$-$]

Pr = Prandtl number [$-$]

$$Re = \frac{\rho u_m D}{\mu} \tag{4.9}$$

where:

ρ = Fluid density [$\frac{kg}{m^3}$]

u_m = Average fluid velocity [$\frac{m}{s}$]

μ = Dynamic viscosity of the fluid [$\frac{kg}{m*s}$]

$$Pr = \frac{\mu C_p}{\lambda_f} \tag{4.10}$$

where:

C_p = Fluid specific heat capacity [$\frac{J}{kg*K}$]

The thermal resistance trough the heat collector pipe wall can be calculated with equation 4.11.

$$R_p = \frac{ln(\frac{r_o}{r_i})}{2\pi\lambda_p} \tag{4.11}$$

where:

R_p = Thermal resistance trough pipe wall [$\frac{K*m}{W}$]

r_o = Radius of the outer wall of the pipe [m]

r_i = Radius of the inner wall of the pipe [m]

λ_p = Thermal conductivity of the pipe wall [$\frac{J}{kg*K}$]

There are multiple methods to calculate the thermal resistance of the borehole fill (groundwater or grout). Below are two examples: Equation 4.13 by Hellström (1991) and Equation 4.12 by Paul (1996) .

$$R_g = \frac{1}{\beta_0 (r_b/r_o)^{\beta_1} \lambda_g} \tag{4.12}$$

where:

R_g = Thermal resistance of the borehole fill [$\frac{K*m}{W}$]

β_0 & β_1 = Best fit parameters

r_b = Radius of the borehole [m]

λ_g = Thermal conductivity of the borehole fill material [$\frac{J}{kg*K}$]

Equation 4.13 shows the Hellström method.

$$R_g = \frac{1}{4\pi\lambda_g}[ln(\frac{r_b}{r_o}) + ln(\frac{r_b}{2x_c}) + \sigma ln(\frac{(r_b/x_c)^4}{(r_b/x_c)^4 - 1})] \tag{4.13}$$

where:

x_c = Half of the center to center distance between inflow and outflow pipe [m]

σ = (λ_g-λ_s)/(λ_g+λ_s) [−]

If the thermal resistance between inflow and outflow pipes are assumed to be the same, the final calculation for the borehole thermal resistance takes the form seen in Equation 4.14.

$$R_b = R_g + \frac{R_f + R_p}{2} \tag{4.14}$$

4.3.2 Measurements

Initial Temperature

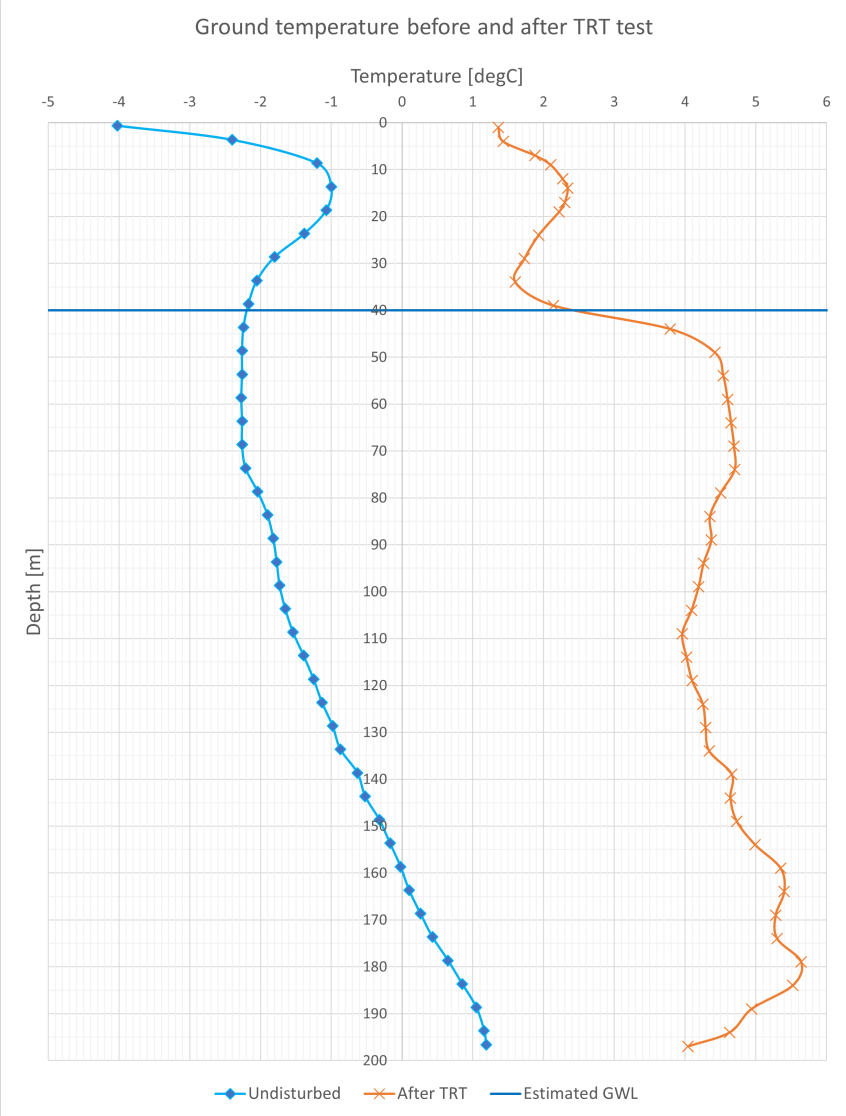

Figure 4.10: Ground temperature before and after the TRT.

Figure 4.10 shows manually measured temperature distribution in the borehole before and after the TRT test. The undisturbed temperature shows warming trend from -4°C to -1°C

between depths of 0 to 15 meters. After 15 meters the temperature starts decreasing until 40 meters, where is estimated groundwater level within the borehole. Between depths of 40 to 70 meters the temperature stays the same, after which it starts to warm as a function of depth. The natural temperature gradient can be seen in the the graph from 100 meters downwards.

The ground temperature curve after the TRT shows similar pattern in the uppermost 35 meters. These values are offsetted by few degrees due to heating from the test. The temperature starts increasing a bit earlier in the 'After TRT' curve, at approximately 35 meters depth. This might be the new groundwater level after the TRT test, if the GWL level has kept risen from the initial estimate of GWL being at -40 m level. The temperature curve shows local high values approximately 4.5°C between 50 to 80 meters depth. After this the temperature drops until 110 meters to 4°C. After 110 meters the graph shows steady increase in temperature until 180 meters depth. Between 180 to 200 meters the temperature drops rapidly. Near the bottom of the borehole, heat has possibility to dissipate not only perpendicular to the borehole wall, but also trough the bottom. This is probably the reason for the rapid decline in the temperature at the end of the borehole.

The changes and temperature fluctuation within the uppermost 40 meters are most likely climate-induced effects due to intra-annual changes.

Heat Carrier Fluid Temperature

Figure 4.11 shows the measured temperature of the heat carrier fluid at inlet, outlet and also the average temperature as a function of time.

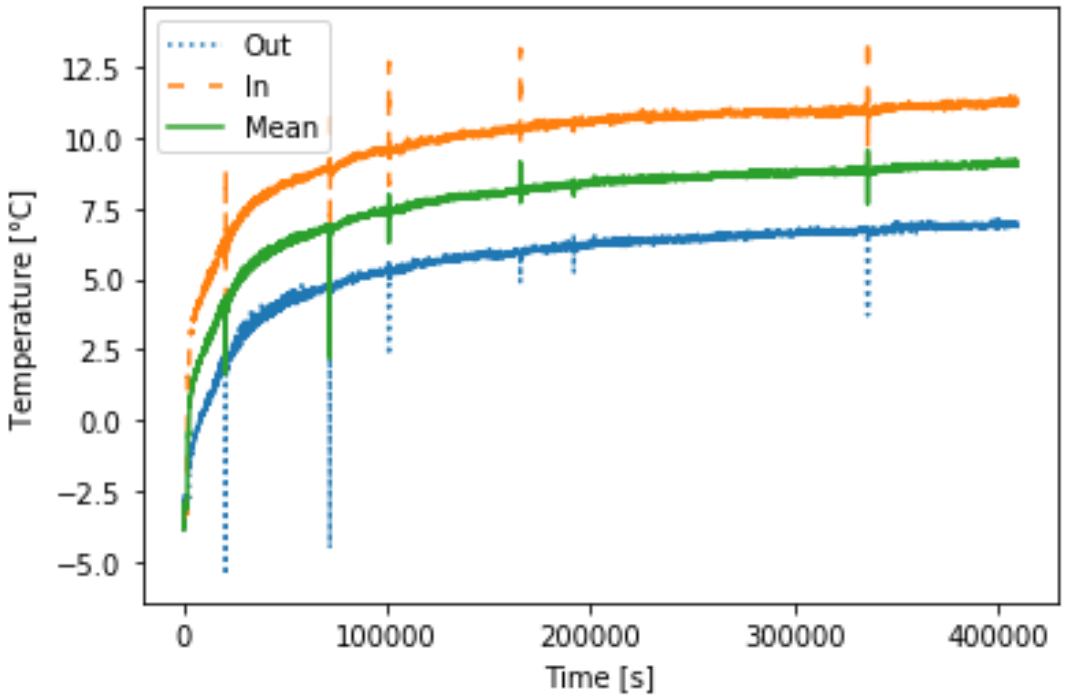

Figure 4.11: Inlet, outlet and average fluid temperature during the TRT. The 6 spikes seen in the curve represent time when the fluid circulating pump was restarted.

As seen in the Figure 4.11, the average fluid temperature grows rapidly in the beginning, until it starts to stabilize after 200,000 seconds. The temperature difference between inlet and outlet is approximately 4°C.

Recovery Phase

Figure 4.12 shows the ground temperature during the recovery. The natural temperature gradient of the bedrock can clearly be seen on in the graph from 100 meters downwards. Gradient being approximately 3 $°C/100m$. Also the groundwater level can be seen at approximately 40 m depth. The reason why the area above GWL is warm is because the air between pipe and borehole wall acts as an insulator, not allowing heat carrier fluid to dissipate the heat into surrounding bedrock as fast as lower part of borehole, which is filled with water.

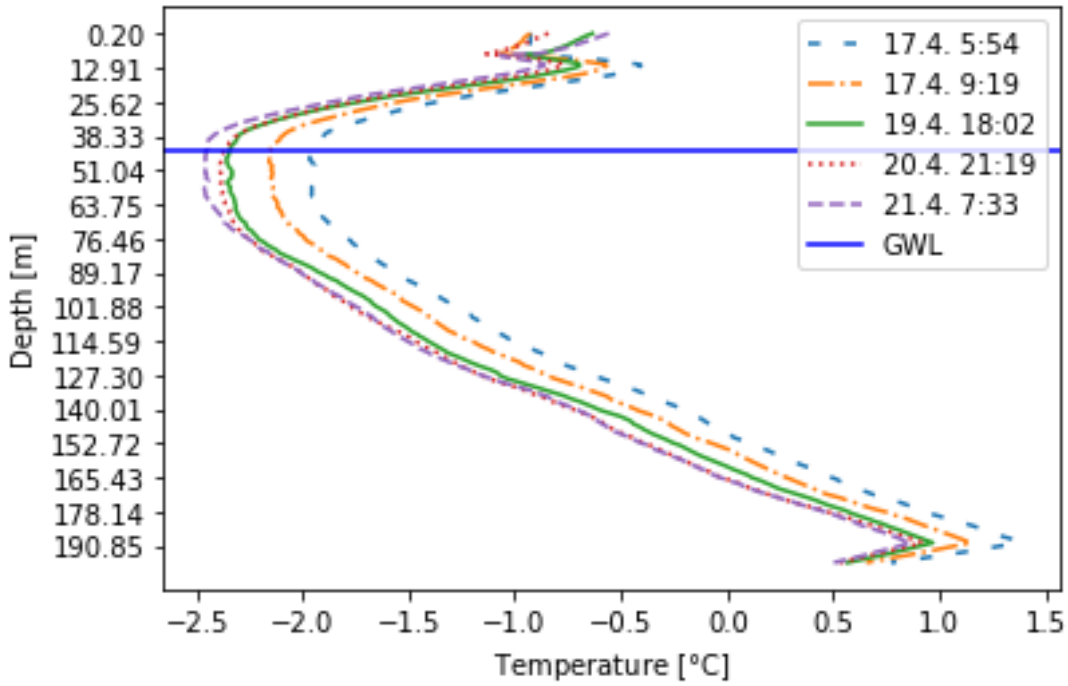

Figure 4.12: Temperatures during the recovery phase.

Distributed TRT

Figure 4.13 shows the temperature distribution within the inflowing collector pipe at five different time steps.

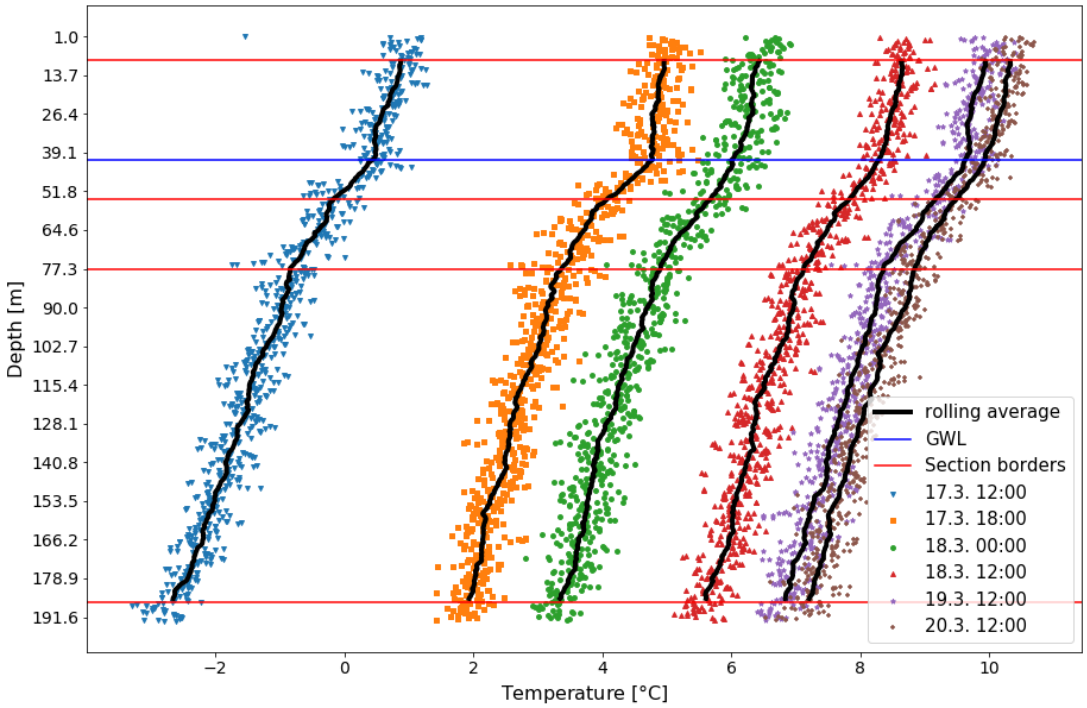

Figure 4.13: DTS measurements from inside the inflowing collector tube. Borehole is divided into four sections with the red lines and GWL.

The curves indicate different time but exhibit a similar trend. The temperature rise within the uppermost 40 meters is slow and steady. However sharp increase in the slope is seen between 40 to 60 meters. Between 60 to 80 meters the temperature is lowering at a slower rate, but faster than the last 100 meters. After 80 meters the temperature change appears to even out, and continues to be stable almost to the end. The temperature difference between individual curves shows that in the beginning the ground temperature changes fast, and it slowers remarkably after few days. The time difference between the first two curves is 6 hours. The temperature difference in the first 6 hours is as large as one shown in the last 60 hours.

4.3.3 Results

Thermal Conductivity and borehole thermal resistance from TRT

Solution of 50 % "Kilfrost GEO" mixed with water was used as heat carrier fluid. The properties of the solution can be seen in table 4.1. Flow rate, temperature difference and the fluid properties, namely heat capacity and density are used to calculate energy transferred into the bedrock. The calculated heating power can be seen in Figure 4.14b.

Table 4.1: Physical and thermal parameters of the heat carrier fluid (50%-vol *Kilfrost GEO* / water) Source: Kilfrost (2021).

Temperature	**Density** $[\frac{g}{cm^3}]$	**Specific heat capacity** $[\frac{kJ}{kg*K}]$	**Thermal conductivity** $[\frac{W}{m*K}]$
20	1.187	3.39	0.414
15	1.189	3.38	0.415
10	1.191	3.37	0.415
5	1.194	3.37	0.416
0	1.195	3.36	0.416
-5	1.199	3.35	0.416
-10	1.201	3.35	0.417

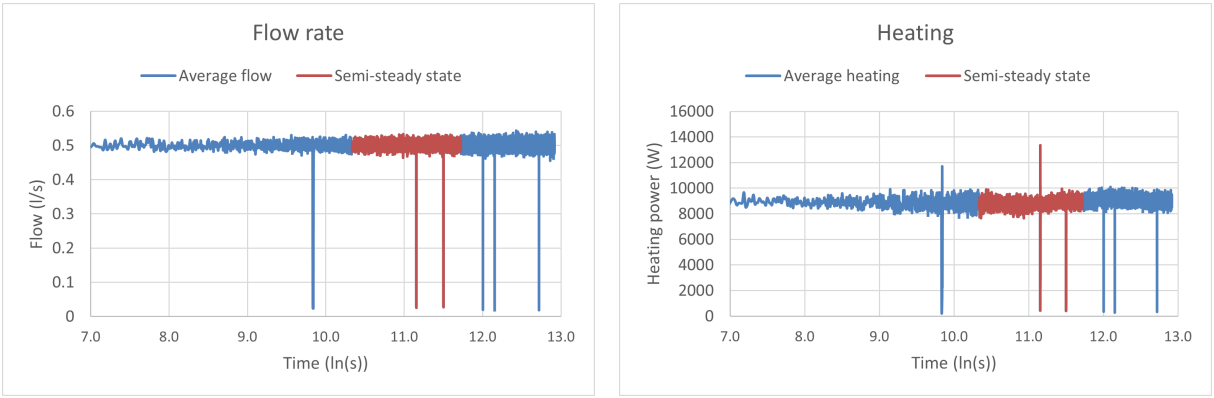

(a) Recorded flow rate.

(b) Average heating power calculated using measured temperatures at inlet and outlet and flow rate.

Figure 4.14: Heating power and flow rate during the TRT.

Figure 4.14 shows the measured flow rate of the heat carrier fluid, and heating power calculated from the flow rate and the temperature difference between inlet and outlet temperatures (see equation 4.4). As seen, both of them are relatively constant throughout the test. The six spikes occur when the circulation pump was restarted. The flow rate is approximately 0.5 litres per second, and the heating power near 9 kW. Figure 4.15 shows the trendline where slope k is determined from.

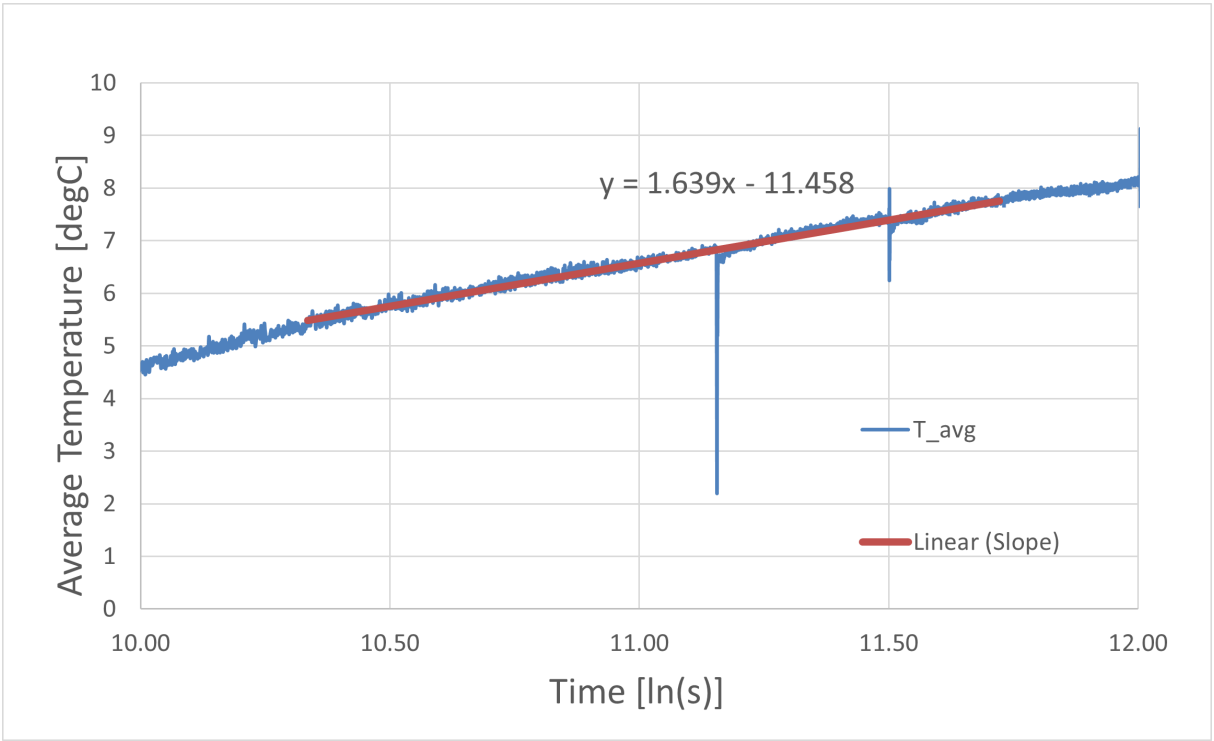

Figure 4.15: Quasi steady state section of TRT from where the thermal conductivity is determined.

The results calculated from the TRT are:

$\lambda = 3.05 \frac{W}{m*K}$ and $R_b = 0.9 \frac{K*m}{W}$

Thermal conductivity determined from the TRT test is reasonable and falls within the range of values found in literature. The value is on the higher end, but this is expected due to high quartz content within the rock. The borehole thermal resistance is also in line with the values found in literature. Table 4.2 shows the results for theoretical estimates.

Table 4.2: Analytically determined borehole thermal resistance.

Component		**Value**
R_f		0.015
R_p		0.048
R_g	Hellström	0.087-0.19
	Paul	0.11-0.22
Total		**0.12-0.26**

The theoretical estimate of borehole thermal resistance is 0.12 $\frac{K*m}{W}$ with the most optimal, and up to 0.26 $\frac{K*m}{W}$ in the most unoptimal collector positioning. These values are higher compared to the value retrieved from the TRT, but this is expected result. Hakala et al. (2014) notes that the analytical methods might overestimate the borehole thermal resistance due to natural convection within the groundwater.

Thermal Conductivity from DTRT

The borehole was divided into four sections according to figure 4.13. Corresponding thermal conductivities are shown in table 4.3.

Table 4.3: Results from the DTRT.

Depth [m]	**Thermal conductivity [$\frac{W}{m*K}$]**
5 - 41	2.31
41 - 56	5.27
56 - 77	4.16
77 - 186	3.5
Mean	**3.4**

Results from the Distributed TRT show difference in the thermal conductivity along the depth of the borehole. It appears that the thermal conductivity is at highest in 41 - 56 m and 56 - 77 m depths with corresponding values of 5.3 and 4.2 $\frac{W}{m*k}$. Lower value in the top part of the borehole is reasonable with the assumption of top section of borehole not filled with water. However this is still valuable information. It could be that when the permafrost

around the borehole thaws, water within the borehole seeps away. In this case grouting could be an option, or operating the BTES with top part filled with air, however this way the system would not be working optimally. On the other hand layer with low thermal conductivity could act as a natural insulation in the top part of BTES, decreasing heat losses trough the ground surface. However the energy saved this way is probably not enough to justify the increased cost from limited capacity.

Ground Thermal Regime

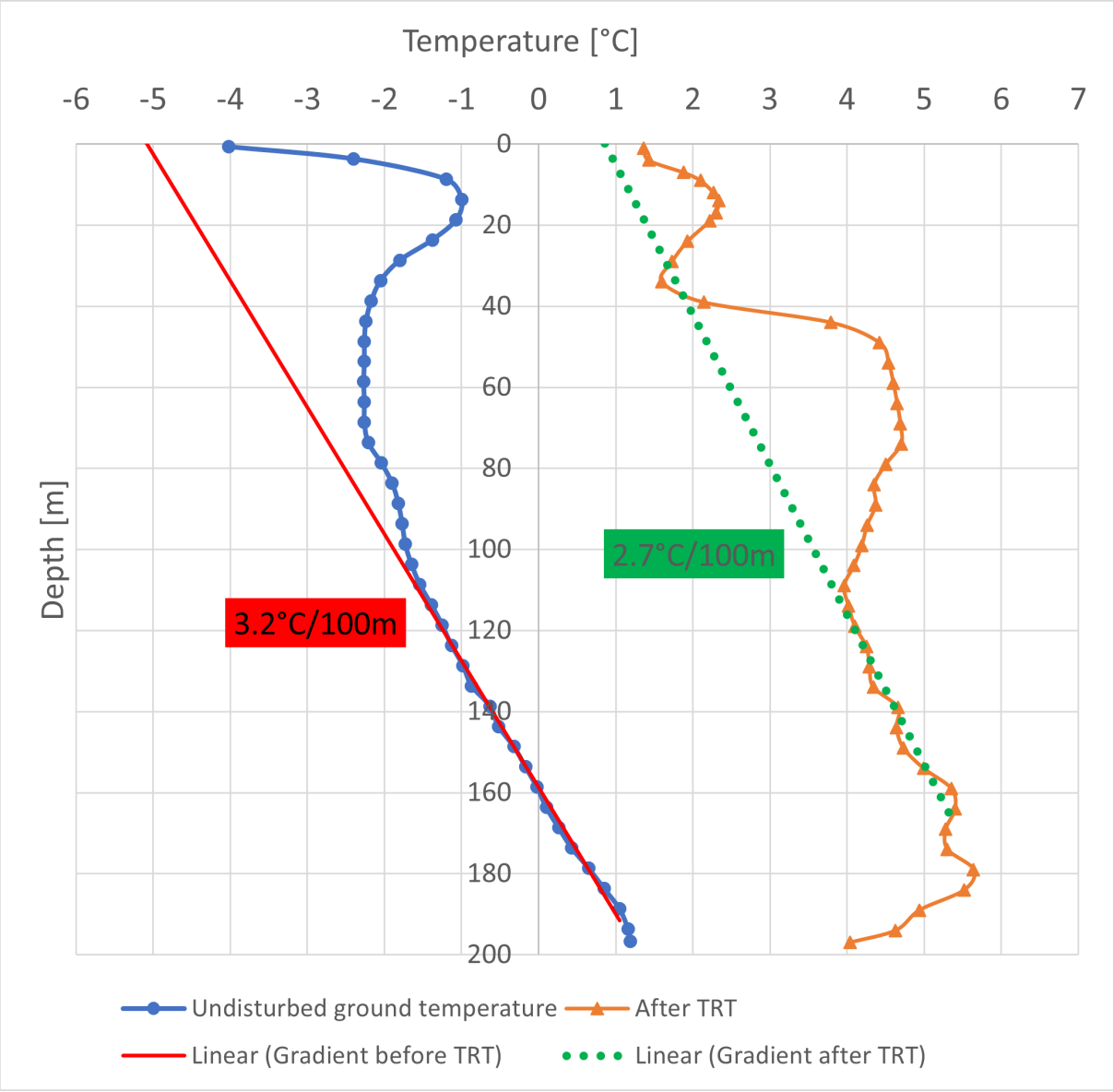

Figure 4.16: Temperature gradient determined from the ground temperature measurements before and after TRT.

Temperature gradient determined from the undisturbed ground temperature shows value of 3.2 $°C/100m$. Gradient determined from temperature measurements done after the TRT provided results 2.5 - 2.8 $°C/100m$. The temperature gradient determined from the temperature during recovery time-series (see figure 4.12) show even higher temperature gradient of 3.5 $°C/100m$.

4.3.4 Limitations

The exact position of collector within the borehole is unknown. Differences seen in the DTRT could be (at least partly) also due to spacing in the borehole. Some sections of the collector might be touching the borehole wall, having high heat transfer rate thus showing high thermal conductivity. In other sections the collector might be close to the middle of the borehole, showing opposite results. This could be partly limited by using spacers in between the inflow and outflow pipes. Figure 4.17 illustrates this issue.

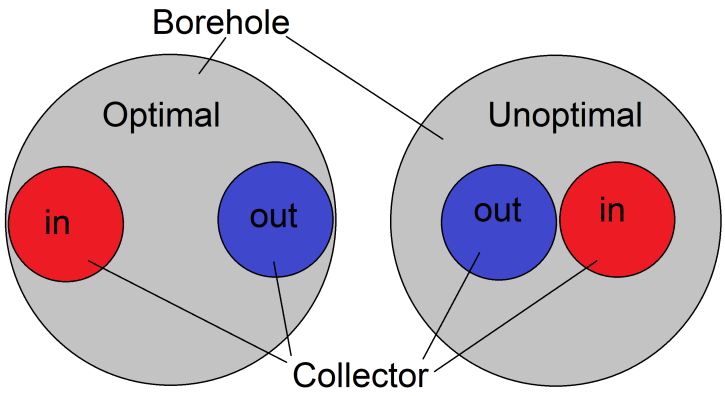

Figure 4.17: Schematic showing optimal and sub-optimal collector positioning within the borehole.

Wind speeds started growing in Longyearbyen during the test, reaching storm scale values. Since the TRT rig is not that heavy, and it has a large flat surface area, fear arised that it would topple from the force of the winds. This was eliminated by acnhoring the rig into the top part of the borehole and a concrete weight from the other side. After the test had ended and the rig was taken away, datalogger was left on site to record ground temperatures during the recovery phase. The logger was inside a zarges box, and the metallic zarges was covered with a wooden box turned upside down. Regardless of the measures taken, small amount of snow found a way into the box where the datalogger was stationed, exposing it to errors and malfunctioning. These examples are not necessarily related to the testing methods itself, but provide a unique perspective to issues and limitations arising from operating in the high arctic environment.

Chapter 5

Numerical modelling

This chapter explains the creation of the numerical model. Chapter starts with the initial data and dimensioning of the BTES system. It then explains the selection of parameters used in the simulation. Finally results are collected and discussed.

5.1 Initial data

The basis for dimensioning and simulation of the BTES system is the annual heat demand in Longyearbyen. From the total heat produced, the amount which can not be produced with solar collectors in certain time period has to be extracted from the BTES. The current production is discussed in chapter 2.

Energy Production

Data set of district heating production was received from the local government. The data set consisted of hourly data of district heating production power in MW. The dataset had values from 01.01.2017 to 20.02.2020. Data was not fully complete and it had some gaps showing unrealistic values such as negative power production. This was discussed with a representative from the power plant and data was patched by interpolating over these corrupted data. After this a standard year was created, with daily average of heating power. Finally a parametric curve was created to further even out the inconsistencies within the data and show the intra-year variation in a more clear way. An illustration of the energy production can be seen in the figure 5.1. The sum of this fitted curve was used as the annual heating demand. The value is 70.67GWh, which represents the true measured values.

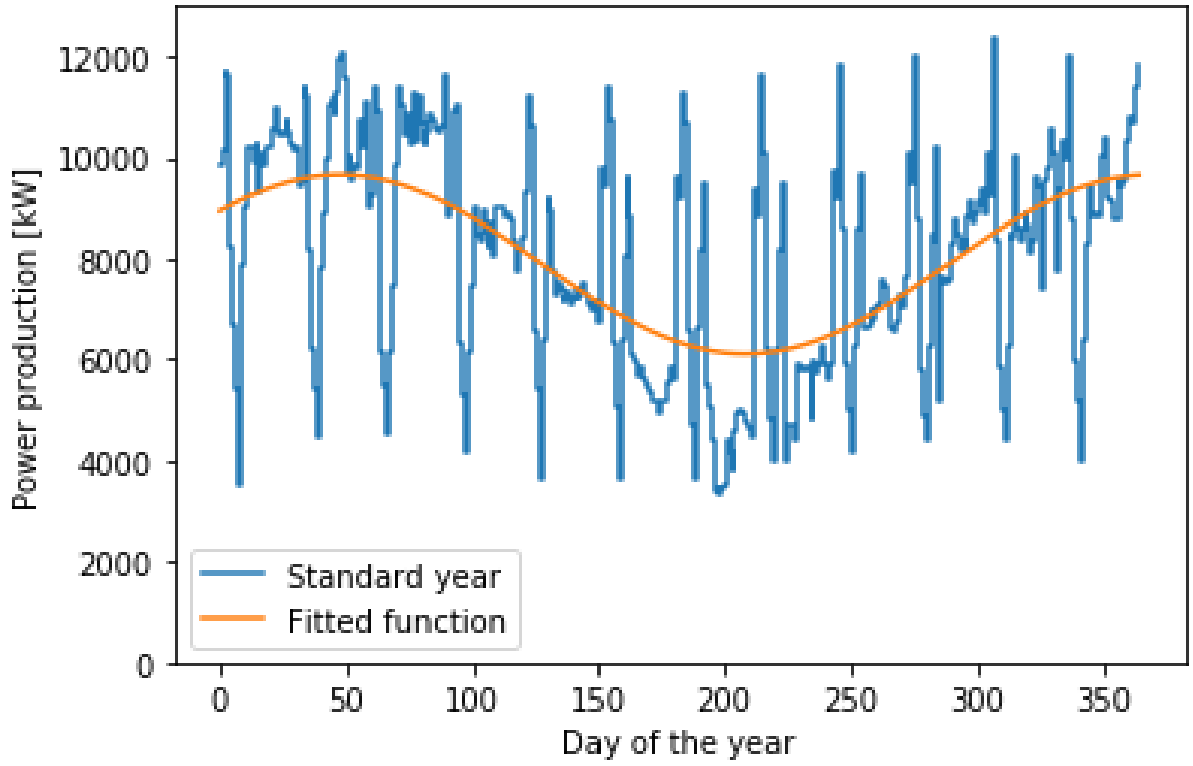

Figure 5.1: Average heating production for years 2017 - 2020.

Heating power fluctuates within 4 - 12 MW range. The average yearly heating power is close to 8 MW. During coldest winter months the heating demand is approximately 10 MW, whereas in warmer summer months it is at 7 MW.

Solar Radiation

UNIS has a measurement station in Adventdalen which logs solar and infrared radiation. The system measures downawrds and upwards radiation, to determine the net radiation affected by albedo. Data is logged in 5min interval and it extends back to 2012. Infrared radiation is disregarded from the dataset. Data included errors such as negative values. This may be caused by calibration error. All the negative values for solar radiation were replaced with zero. Also leap years were disregarded from the data, as 365 day year will be used in the simulation. An average year was created. Fitted curve was created to further smoothen the curve. The average year with the fitted curve can be seen in figure 5.2.

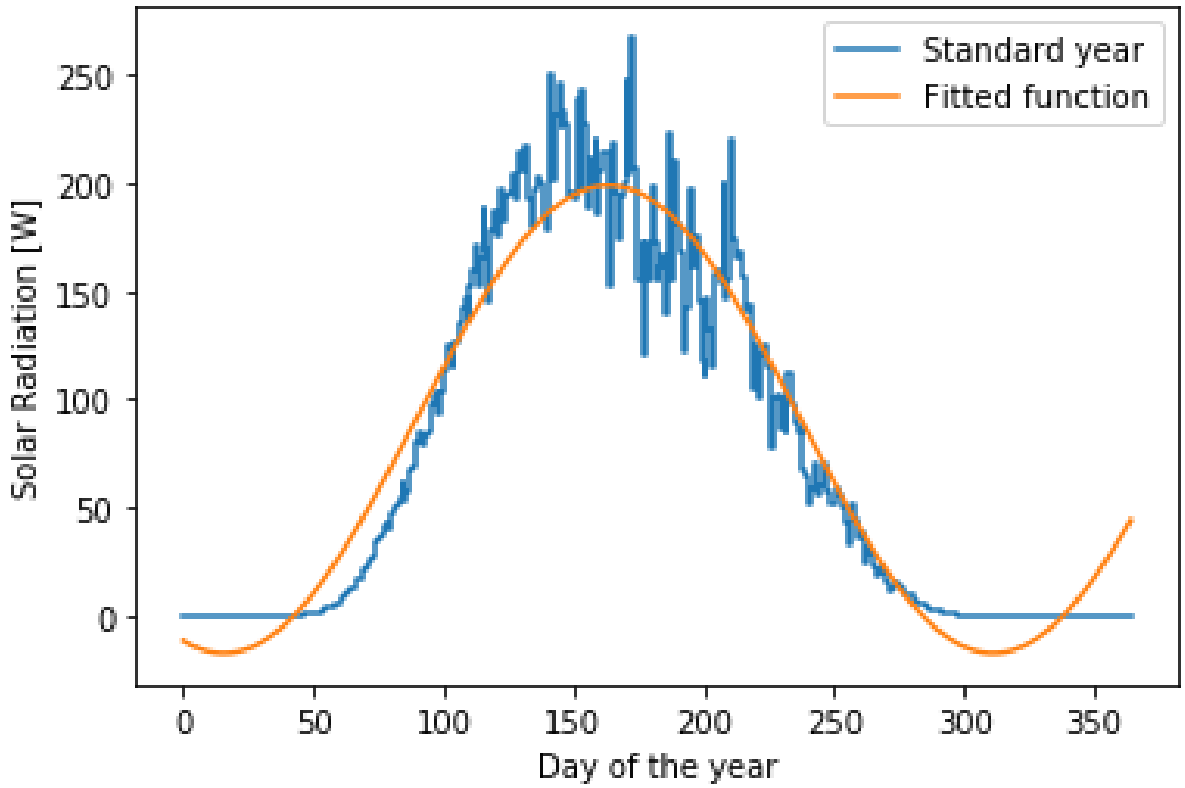

Figure 5.2: Average annual solar radiation per square meter between 2012 and 2021.

As seen in the figure 5.2 the fitted function shows some negative values near the beginning of the year and after 300 days. These values were set to zero, as it is known that there is practically no solar radiation during the polar night.

From the standard year, average yearly energy production was calculated. In the graph this can be seen as the area between the 'standard year' curve and y=0 line. The average annual solar radiation received by 1 m^2 is 644 kWh. By dividing the energy demand with the energy production of one square meter of solar collector, the required area for solar collectors is found. This would be the area needed for solar collectors, to fulfill whole heating demand in Longyearbyen. The needed area is:

$$A = \frac{Q_{heating}}{Q_{solar}} = \frac{70,000,000kWh}{644kWh/m^2} = 108,696m^2 \tag{5.1}$$

All of the radiation can not be turned into usable energy. However since the efficiency of solar collectors varies between the type of the collector e.g. flat plate, glazed/unglazed, evacuated tube etc., an area of 110,000 m^2 is used in the study. This area could be covered with 300 x 400 m rectangle.

5.2 Dimensioning of the BTES

The ground properties at drill site one will be used in the modelling. This is the site where most extensive data is gathered, and the site is in many ways suitable for an actual operating BTES site aswell. Dimensioning of the BTES goes as follows: First the amount of energy needed to be stored has to be determined. This is done by summing the daily surplus energy from the solar collectors during the year. The production from the solar collectors is greater than the heating demand for 163 days a year, from approximately April to mid October. The surplus energy is the positive values when deducting daily energy production of solar collectors from the daily energy demand. The value is 37.5 GWh, which stand for 54 % of the annual heating. Surplus energy, which is injected into the bedrock during charging period is shown in figure 5.3 in pink colour and labelled “Charging”.

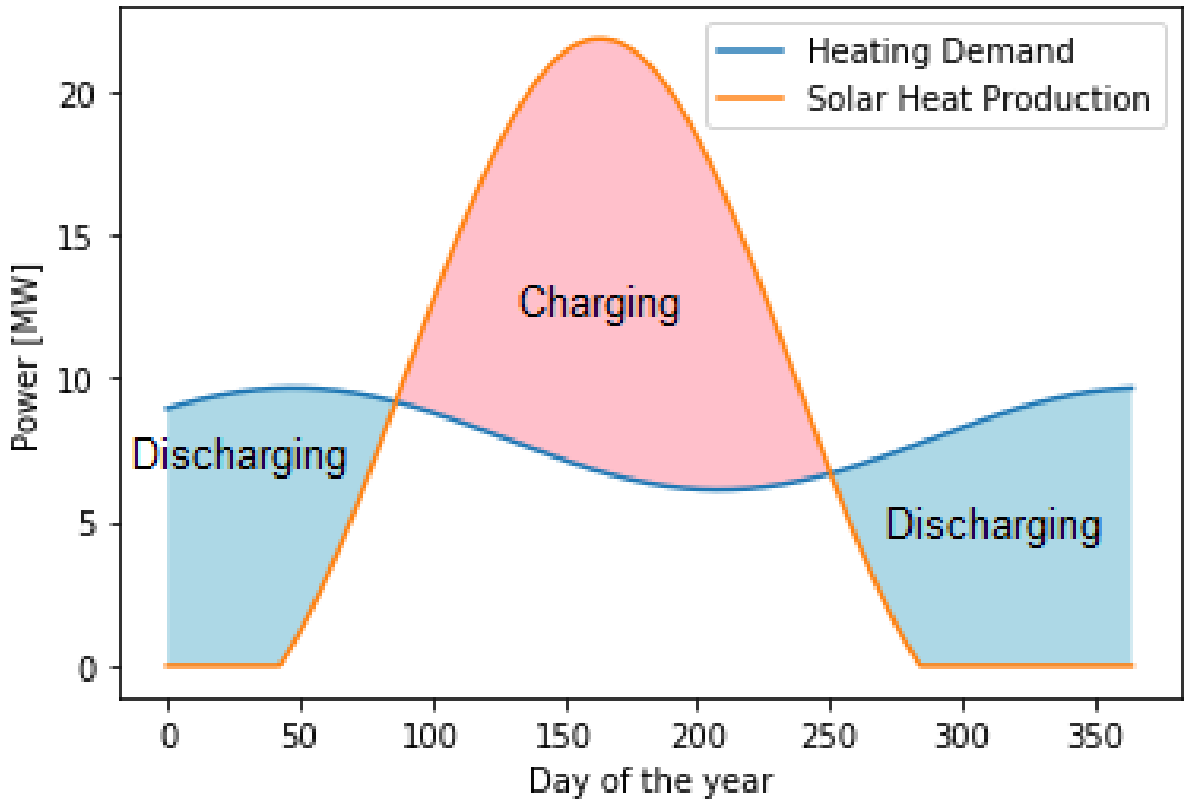

Figure 5.3: Heating demand and heating power production.

Volume of the BTES can be calculated, if the specific heat capacity (C_p), density of the rock material (ρ), operating temperature difference (ΔT) and energy Q are known (shown in equation 5.2).

$$\begin{aligned} Q &= C_p \rho V \Delta T \\ => V &= \frac{Q}{C_p \rho \Delta T} \end{aligned} \tag{5.2}$$

Operating temperature is set to 50 °C. This is the temperature difference during the operation of the BTES, meaning that in the end of charging period in late summer, the temperature would be 50 degrees higher than at the beginning of charging (late spring). 50 degree temperature difference in permafrost areas in Longyearbyen would mean highest temperature approximately +50 °C or little higher. Higher temperature will not be used due to technical limitations discussed in section 3.2. Plastic collector tubes can not handle long term temperatures over 70°C.

Table 5.1: Temperature limitations for plastic pipes. Table edited from Reuss (2015). Original values from standard VDI 4640 Part 2; 2014

Material	**Continuous operating temperature for 50 years**	**Peak temperature during 1 year**	**Thermal conductivity** $[\frac{W}{m*K}]$
PE100	40°C at 11.6 bar	70°C at 6.2 bar	0.42
PE100-RC	40°C at 11.6 bar	70°C at 6.2 bar	0.42
PR-RT	70°C at 6.5 bar	95°C at 8.1 bar	0.42
PA	40°C	70°C	0.24
PB	70°C at 12.1 bar	95°C at 8.1 bar	0.22
PE-X	70°C at 8.5 bar	95°C at 6.8 bar	0.41

Also high temperature difference between the collector fluid and borehole wall is needed to ensure sufficient heat transfer rate. According to table 5.1 this would leave 20°C margin for temperature difference between collector fluid and borehole wall in continuous operation, or 45°C short-term when using PE-RT pipes which are meant for high temperatures.

Heat capacity and density of the bedrock are estimated from literature. Table 5.2 shows various literature values for physical and thermal properties of sandstone. Density of 2,600 $\frac{kg}{m^3}$ and heat capacity of 800 $\frac{J}{kg*K}$ is chosen.

Table 5.2: Physical and thermal parameters of rock formations containing sandstone.

Thermal conductivity $[\frac{W}{m*K}]$	**Density** $[\frac{g}{cm^3}]$	**Heat capacity** $[\frac{kJ}{kg*K}]$	**Source**	**Notes**
3.0	2.8	-	Côté and Konrad (2005a)	
3.4	2.67	-	Côté and Konrad (2005b)	
3.5 [1] 2.9 [2] 2.6 [2]	-	-	Liebel (2012)	[1] TRT measurements [2] Lab measurements
3.3	-	-	Midttømme et al. (2004)	
0.81 - 1.63 [3] 2.25 - 2.47 [4]	2.27 [3] 2.62 [4]	0.82 - 0.92 [3] 0.79 - 0.81 [4]	Xiong et al. (2020)	[3] Coarse, Cretaceous [4] Fine, Triassic
2.6 [5] 2.8 [6] 3.4 [7]	-	-	Ramstad et al. (2014)	[5]Cambrian to Ordovician age [6] early Silurian age [7] late Silurian age
1.9 - 4.6	2.2 - 2.7	0.67 - 1.23 [8]	Reuss (2015)	[8] Calculated from volumetric heat capacity

With the determined parameters, the resulting volume for BTES is $V = 1,300,000m^3$.

With borehole depth of 200m the required surface area is $6,500m^2$. With a square pattern that would make approximately 81x81m. Borehole spacing is dependant on the thermal properties of the ground. In conventional geothermal heating systems the spacing should not be too close, so that the heat extraction in one borehole does not affect the heat extracted from another. However in energy storage, where heat is constantly injected and extracted it does not matter as much. Also since the dimensioning is based on assumption that the borehole is able to heat up the whole medium meaning that there should virtually be no temperature difference between two boreholes. Optimal solution would be to have as few boreholes as possible. However the fewer boreholes there are, the higher the heat transfer per borehole. If heat flow between the collector fluid and bedrock is too high in relation to the heat conductivity and thermal diffusivity of the storage medium, the heat does not dissipate fast enough and the area immediately around the borehole will start to warm up fast. High heat transfer requires high temperature difference, and as discussed previously, there are temperature limitations regarding the system

5.3 COMSOL

5.3.1 Creation of the Model

Heat transfer in solids is used to model the system. Time-dependant analysis is done to analyse inter and intra year variations. The model builder tree can be seen in figure 5.4. It is divided into Global definitions, Components and Study. Geometries, physics, and materials are determined from within the component tree.

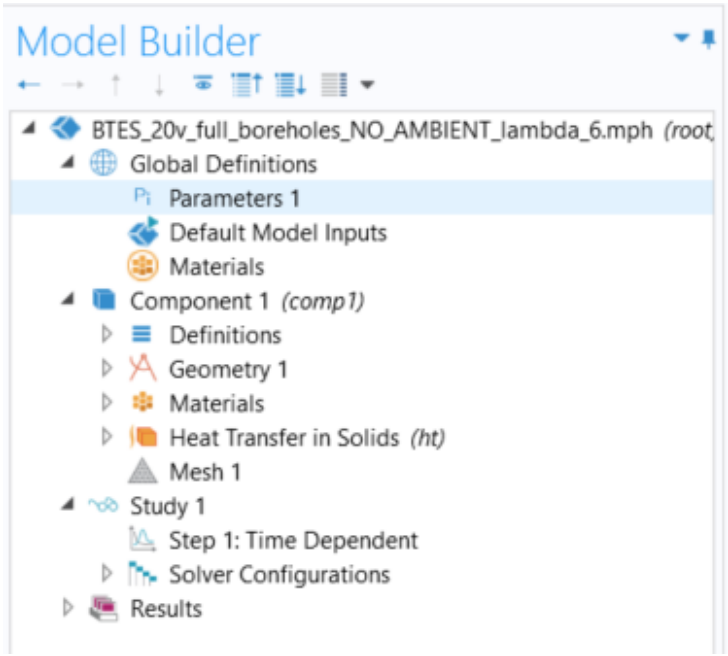

Figure 5.4: Example of COMSOL model builder.

Geometry

Comsol works well with most CAD softwares, enabling importing of pre-created geometry. However the model created in this work is simple, so that it can be easily created within the comsol itself.

Comsol allows the save of parameters, which can be accessed any time during the modelling. Most relevant functions and parameters are saved here. This is extremely helpful for example when the model needs to be edited or iterated. Instead of re-drawing multiple functions and values, it might be that only one parameter has to be edited. The global parameters can be seen in figure 5.5

Parameters

Name	Expression	Value	Description
bh_n	17	17	n of boreholes in y-direction
dist	5[m]	5 m	Borehole distance
diameter	bh_n*dist+100	185 m	Domain radius
bh_depth	-200[m]	-200 m	Depth of boreholes
domain_depth	bh_depth-100	-300 m	Depth of domain

Figure 5.5: Global parameters for the model.

For simulation of the BTES and surrounding environment, cylindrical domain was modelled in 3D. Height and diameter of the domain were given as parameters related to the size of the actual storage (volume lined by borehole extremities).

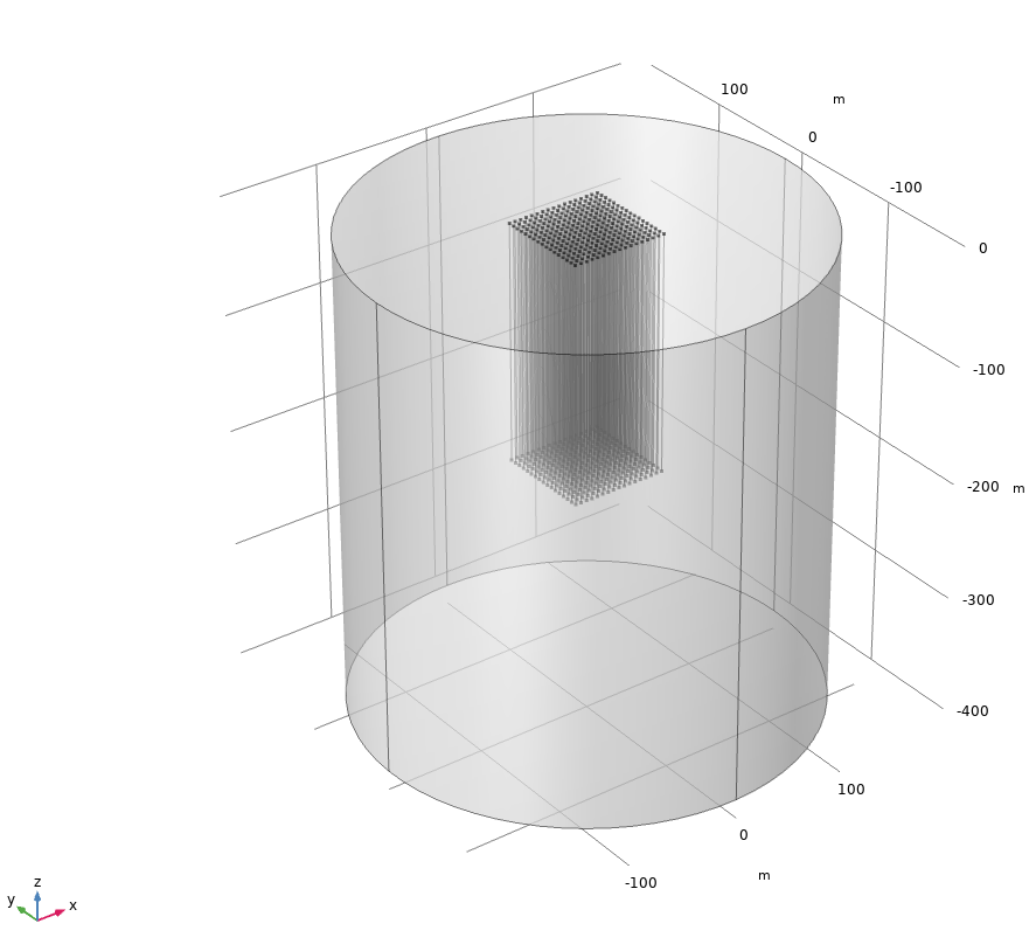

Figure 5.6: 3D representation of the model.

Borehole heat exchangers were simulated as line heat sources. Due to high number of BHEs it was not efficient to create each of them individually. Instead one borehole (1D line

modeling BHE) was created as an 'interpolated curve'. This line was then multiplied with an 'array' command in Comsol. The array receives number of final units, spacing, and direction as an input. The borehole field was created in a quadrical pattern for simplicity. Borehole spacing of 5 meters was used in the beginning, but this was later iterated to find optimal solution (see section 5.3.2).

Material for the BTES medium was created as homogeneous sandstone. Material properties are the same throughout the domain. The material parameters can be seen in figure 5.7

Material Contents

	Property	Variable	Value	Unit	Property group
☑	Thermal conductivity	k_iso ;...	lambda_1	W/(m·K)	Basic
☑	Density	rho	2600	kg/m³	Basic
☑	Heat capacity at constant pres...	Cp	800	J/(kg·K)	Basic

Figure 5.7: Material properties assigned for the model.

Boundary Conditions

First boundary condition is the surface temperature. Average weather data from Svalbard Airport was used as the upper boundary condition. This was retrieved from AASHRAE database of Comsol.

Geothermal heat flux is assigned to the bottom surface. Heat flux is given a value of 0.07 W/m^2 as it is found to be the in-situ heat flux within the area, as presented in section 2.2.

The total heat rate is calculated from the difference between heat production and heat demand, which is illustrated in figure 5.3. This value has to be divided by the amount of boreholes to get heat rate per borehole, and divided by borehole depth, to get the final value of heat per (borehole) meter with a unit of W/m. Positive values are heat injection, and negative values for heat extraction. The heat rate per borehole meter is shown in the figure 5.8.

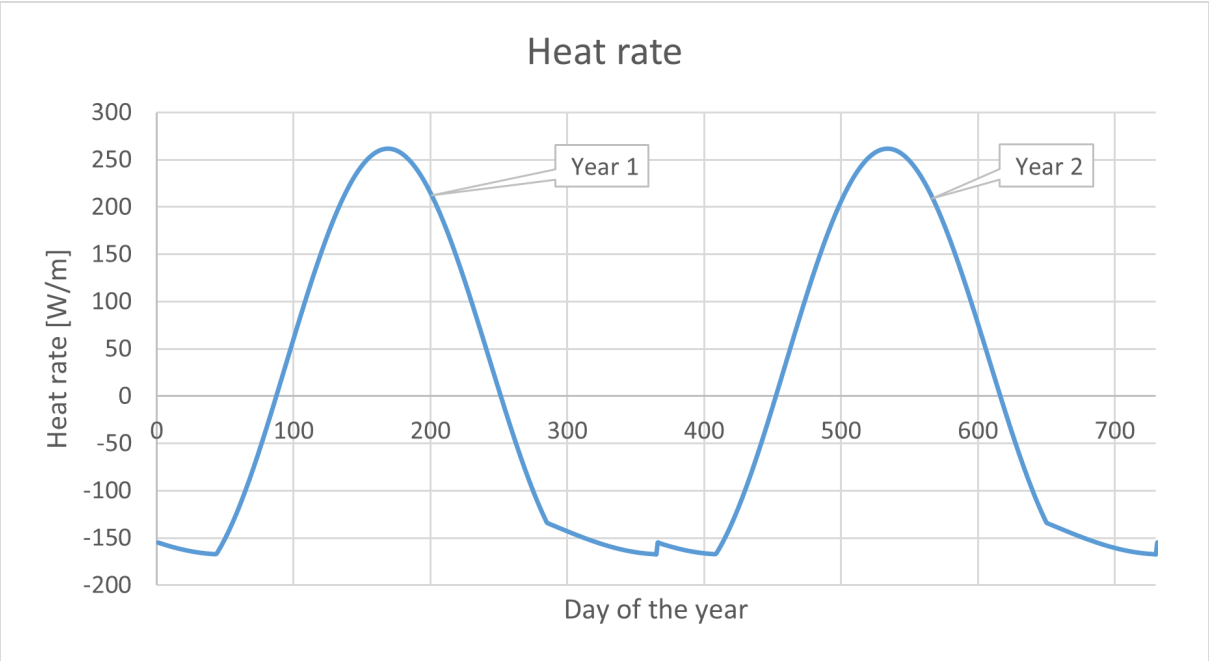

Figure 5.8: Heat rate assigned for each borehole.

Parameters

To perform the simulation, material parameters have to be given. In the *Heat Transfer in Solids* -module of COMSOL, required parameters are density, thermal conductivity, and heat capacity. Thermal conductivity of 3.0 $W/m*K$ was chosen as it is the result from the TRT test. Also this value corresponds well with values from literature and thermal conductivity estimate based on mineralogical content of drill cuttings. Heat capacity was given as 800 $J/kg*K$ and density of 2,600 kg/m^3, which are from the literature.

Initial temperature for the domain was given as the heat gradient. Heat gradient was given starting from the ground surface, even as the top tens of meters experience seasonal variation. However the same gradient of 0.03°C/m was given for the whole domain to simplify the modelling.

5.3.2 Results

Borehole spacing, heat rate, ramp up time

Figure 5.9 shows the results from the first simulation with 17 x 17 boreholes having a 5 meter spacing.

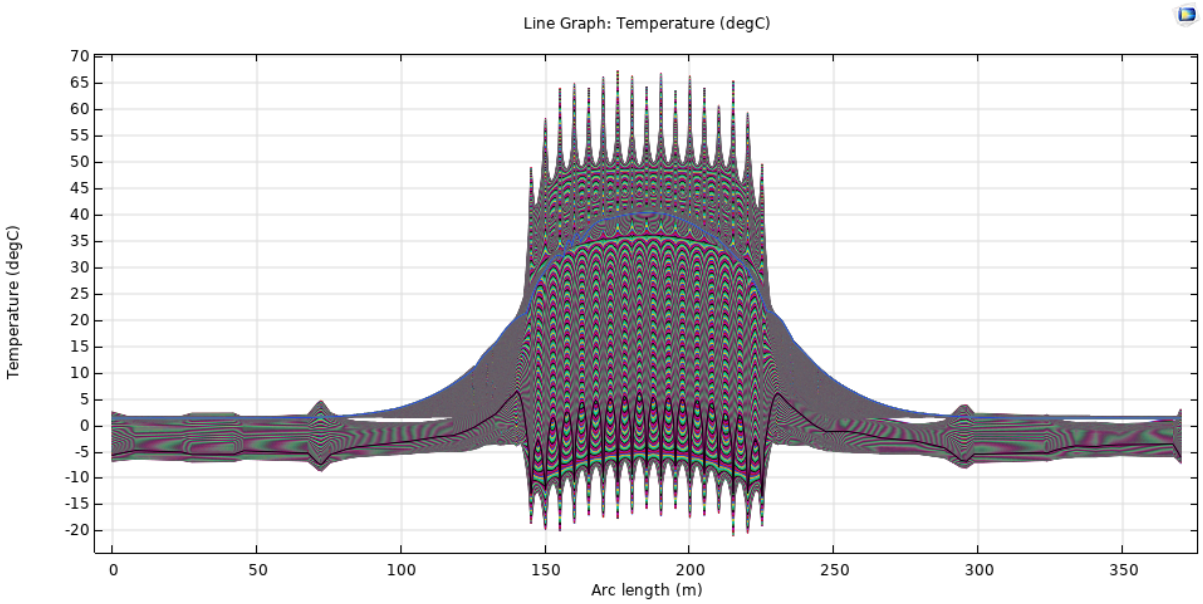

Figure 5.9: Temperature profile over 20 year simulation period with 17x17 boreholes. Temperatures are plotted along a cut line aligned with x-axis at -50 m depth. The spikes in the temperature show the location of the boreholes.

As seen the temperature immediately adjacent to the boreholes differs by over 15 °C from the surrounding medium. This indicates that the heat rate in the borehole is too high compared to the thermal conductivity of the storage medium. The bedrock next to the borehole heat exchangers can not conduct the heat away from the BHE fast enough, causing the temperature in the immediate vicinity to the borehole to increase too much. The maximum heat rate with the 17x17 borehole setup is 260 W/m, which is a high value. Typically the heat rate within the GHE is tens of watts per meter.

The second simulation was run with 22x22 boreholes. With the increased amount of boreholes, the maximum heat rate is now 150 W/m. The spacing between the boreholes is kept in 5 meters. Results can be seen in figure 5.10. The top left graph shows the results without "preloading" of the storage. This means that after first summer charging period, the next winter heat is already withdrawn from the storage. The top right picture shows situation with 3 years preloading. The last graph on the bottom shows the results with 2 years of preloading.

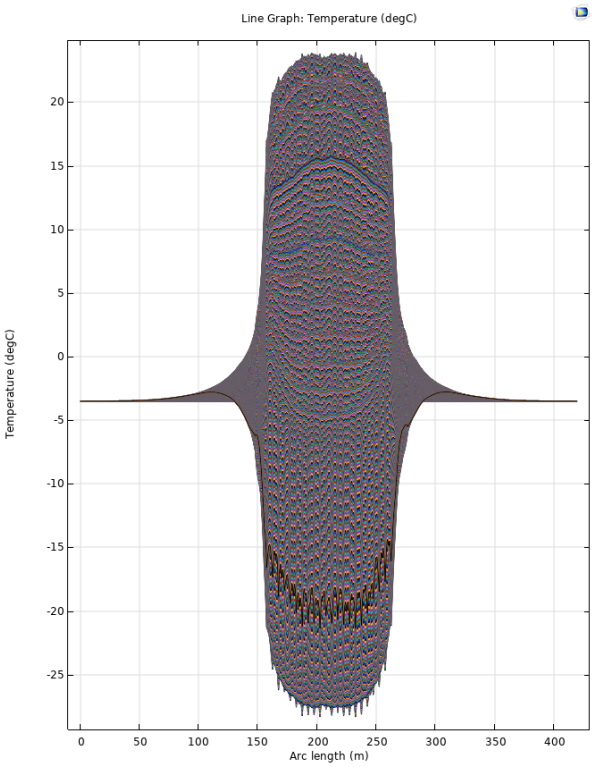

(a) No loading.

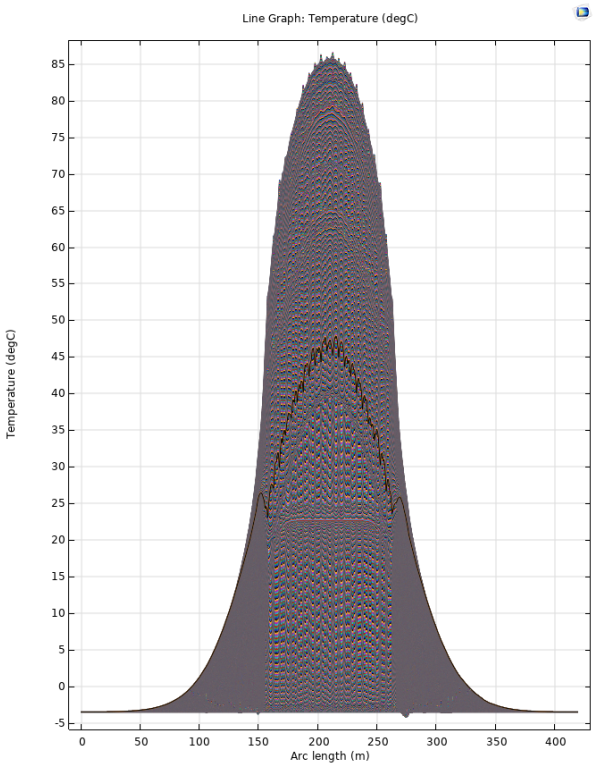

(b) 3 years perloading.

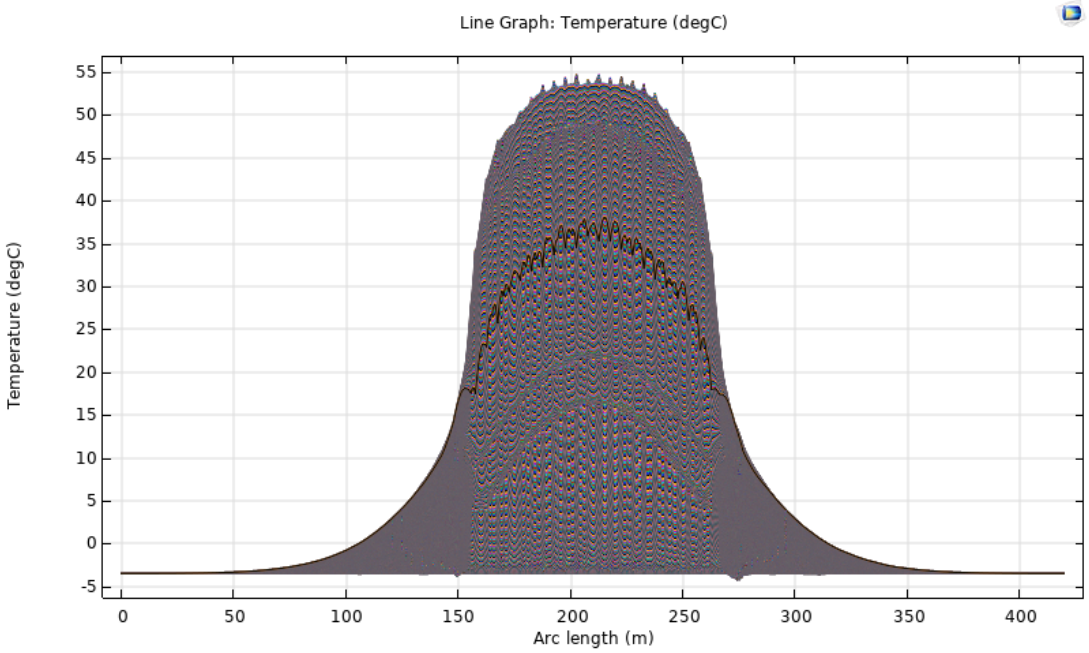

(c) 2 years preloading.

Figure 5.10: Temperature profiles with 0, 2 or 3 years preloading before operation. Each figure shows temperature profile for every day during 20 years simulation time.

Subfigure 5.10a shows that the temperature in the BTES drops to negative degrees during heat extraction. The profile shows that the temperature of the storage oscillates approximately between +20 to -25. Negative temperatures cause freezing of the storage, which might be problematic especially in water filled boreholes. Also repeated freezing-thawing cycles

could break and weather the rock.

The temperature of the storage rises too high if the system is preloaded for three conescutive years before first heat extraction. This can be seen in figure 5.10b where the temperature in the first years is as high as 85°C. The end effects can also be seen here, as the shape of the temperature profile is sharp. This shows that the temperature at the center of the storage is higher compared to boundary areas.

Two years of pre-loading appears to be near optimal. The temperature does not grow too high, but it is enough buffer to eliminate freezing during the normal operation of the system, as shown in figure 5.10c. The temperature profile grows near 55 °C, but this happens only during the third or fourth year. The normal operating temperature range stays under 50 °C.

Efficiency

A more detailed model is created according to the results from DTRT which are shown in section 4.3.3. This model was simulated for 20 years with the same borehole configuration and boundary conditions as the first model with homogeneous storage medium. Figure 5.11 shows the temperature profile at the end of charging and discharging phases during different years.

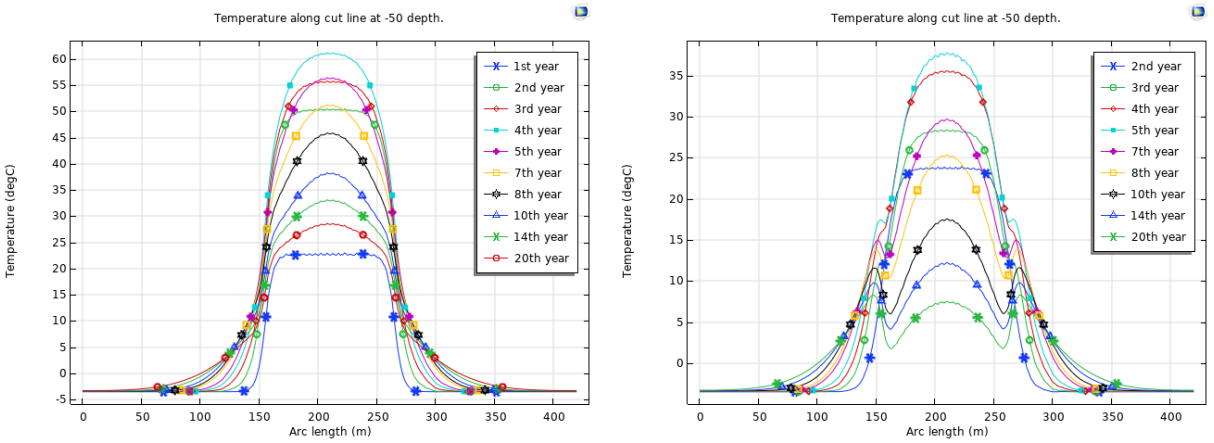

(a) End of charging.

(b) End of discharging.

Figure 5.11: Temperature profile during different years at 50 m depth. Decrease in the storage temperature after the initial preloading phase can clearly be seen.

Both of the graphs 5.11a and 5.11b show that for the first four years the temperature in the storage increases. This is expected due to the preloading phase. However starting from year 5 the temperature keeps dropping until the end of simulation at 20 years. The speed of the temperature change slows down, indicating that it might reach equilibrium at some point. The redution in the storage temperature over time may be caused by heat losses trough the

surface, sides and bottom of the BTES. To reach equilibrium, heat input into the system should be increased while keeping the heat extraction the same level until the temperature stays stable throughout the years. This would allow to determine the efficiency of the system. The current heat injection and extraction ratio indicates that the efficiency is less than 95 %.

Effects on ground thermal regime of the surrounding environment

One of the most important aspects is the impact of the BTES to the surrounding environment. Svalbard including Longyearbyen and surrounding areas are covered in permafrost which is 150 m thick at the proposed site for the BTES (see section 4.1.2). Thermal energy storage is essentially based on increasing the temperature of the storage material, which in this case is permafrost covered soil and bedrock. The heating temperatures surpass the thawing temperature of permafrost by tens of degrees. Concern is how far will the heat from the BTES cascade, as it can have major effects on the land use in areas affected by PF thawing. Figure 5.12 shows the propagation of the 0°C isotherm.

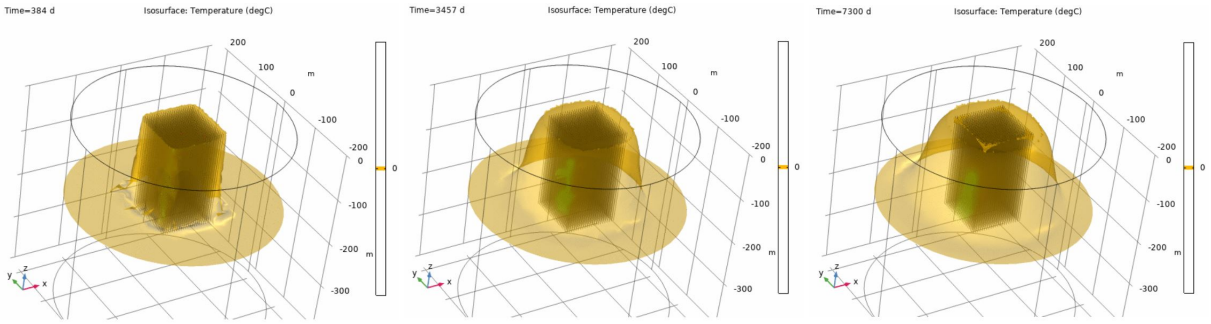

(a) 2nd year. (b) 9th year. (c) 20th year.

Figure 5.12: 0 °C isotherm around the BTES during 2nd, 9th and 20th year of operation. The space on the inside of the surface (close to the boreholes) is higher than 0°C where as the space outside is lower than 0°C.

The figure 5.12 shows how the 0°C isotherm expands outwards from the BTES over time. This illustrates the thawing of the permafrost. The thaw of PF appears to propagate further in the deeper sections compared to ground surface. This is probably due to the natural temperature gradient within the ground and affects from climate, since the MAAT is below 0°C.

5.3.3 Limitations

Using the line heat source to simulate borehole is simple and easy to use method. However the drawback is that for example efficiency of the system can not be directly calculated, since the input and output energy is governed by the user. More precise option would to use pipe

flow module of COMSOL and use flow rate and fluid temperature as a parameter instead of just heat rate.

There are limitations regarding modelling of the insulation layer. The bedrock layers are hundreds of meters thick, where as the insulation layer is only 20 cm. Due to this difference, the meshing of XPS might produce errors, since the layer thickness is smaller than the minimum element size. This was flagged by COMSOL and it provided a heads-up warning.

Chapter 6

Economical Feasibility

This chapter briefly analyses and discusses the economical feasibility of BTES coupled with solar heating system. A preliminary price estimate for the produced heat will be calculated. This chapter is divided into three sections, solar collectors, BTES and heat pumps & network. Each section provides information about the capital and operation & maintenance costs.

6.1 Solar collectors

Solar collectors are individually the most expensive component in this system. The total capital costs consists of price of the equipment/technology itself, storage and shipping, installation and comissioning. The area of solar collectors is calculated in section section 5.1 to be 110,000 m^2. Costs for installed solar thermal systems from various sources are compiled into table Table 6.1.

Table 6.1: Capital cost of solar thermal collector, including installation. Unit prices are in original currency, which is transformed into euros for total cost. Currency transfer rate on 14th July 2021 was used for all of the calculations.

Location	**Unit price**	**Total cost [M€]**	**Source**
Canada	497 $/m2	46.47	Rad et al. (2017)
Russia	*200-1160 €/m2	22-127.6	Ratner et al. (2020)
Scotland	700 £/m2	90.09	GREBE (2017)
Finland	280-340 €/m2	30.8-37.4	
Egypt	355 $/m2	39.05	Bany Mousa et al. (2019)
China	370 $/m2	40.7	
Japan	460 $/m2	50.6	
Australia	496 $/m2	54.56	
Belgium	474 $/m2	52.14	
Italy	441 $/m2	48.51	
Canada	475 $/m2	52.25	
Chile	386 $/m2	42.46	
Brazil	372 $/m2	40.92	
USA	518 $/m2	56.98	
China	872 $/m2	82.53	Epp (2020)
Average		**48.72**	

*These are calculated using highest (Austria, Denmark, Canada, France) and lowest (India) LCOE value for large-scale solar collectors from and

The capital price for 110,000 m^2 solar collector field would be between 31 and 90 M€ according to the unit prices of individual countries from the Table 6.1. Average price is 48.72 M€. Differences between countries are due to local and regional factors such as manufacturing prices, shipping and labor costs. According to Bany Mousa et al. (2019) in USA the installation cost constitutes up to 50 % of the total capital costs. Countries with lower labor costs tend to have lower capital costs. Value of 50 M€ is chosen to represent the capital costs of the solar thermal system.

Operational & maintenance costs for solar collector include possible repair, inspection, changing of the heat carrier fluid and cleaning. Since the system is based on circulating fluid, it needs external power, thus electricity prices play part as well. Solar PV and solar collectors might accumulate dust, dirt or snow on the surface. The surfaces need to be cleared to ensure efficient operation, giving rise to an additional O&M cost. O&M costs might have a fixed value tied to the installed capacity, but usually they are represented as a fraction of the capital cost. Table 6.2 below has some estimates of the total O&M costs.

Table 6.2: Estimated operating and maintenance costs for solar thermal collectors.

Location	Price	Cost [k€]	Source
-	0.25-0.5%	125-250	Ratner et al. (2020)
-	0.9-1.8%	450-900	GREBE (2017)
Finland	20 €/m^2	2,200	GREBE (2017)

As seen, the range of Operation & Maintenance cost is large between different sources. The highest estimate is almost 20x as much as the lowest. 1.8% of capital cost is chosen as O&M cost for these calculations. The Finnish 20 €/m2 appears relatively high number as it would contribute to 5.9-7.1% of the capital costs.

6.2 BTES

The initial costs of the BTES system consists from drilling, materials (grout), collectors, heat pumps and connections network. This section focuses only on the construction of GHEs. Rad et al. (2017) estimates the capital cost of BTES to be 116 $/m = 99 €/m. Discussion with a representative from the company which conducted the TRT resulted the rate for drilling of a 200 m deep borehole, and installing the collector to be approximately 100,000 NOK. This transfers to roughly 10 k €. With this rate the price per borehole meter would be 50 €/m.

Figure 6.1 shows specific costs for different sized BTES systems worldwide. A clear trend is seen, where the price per unit of storage volume decreases as the storage size increases.

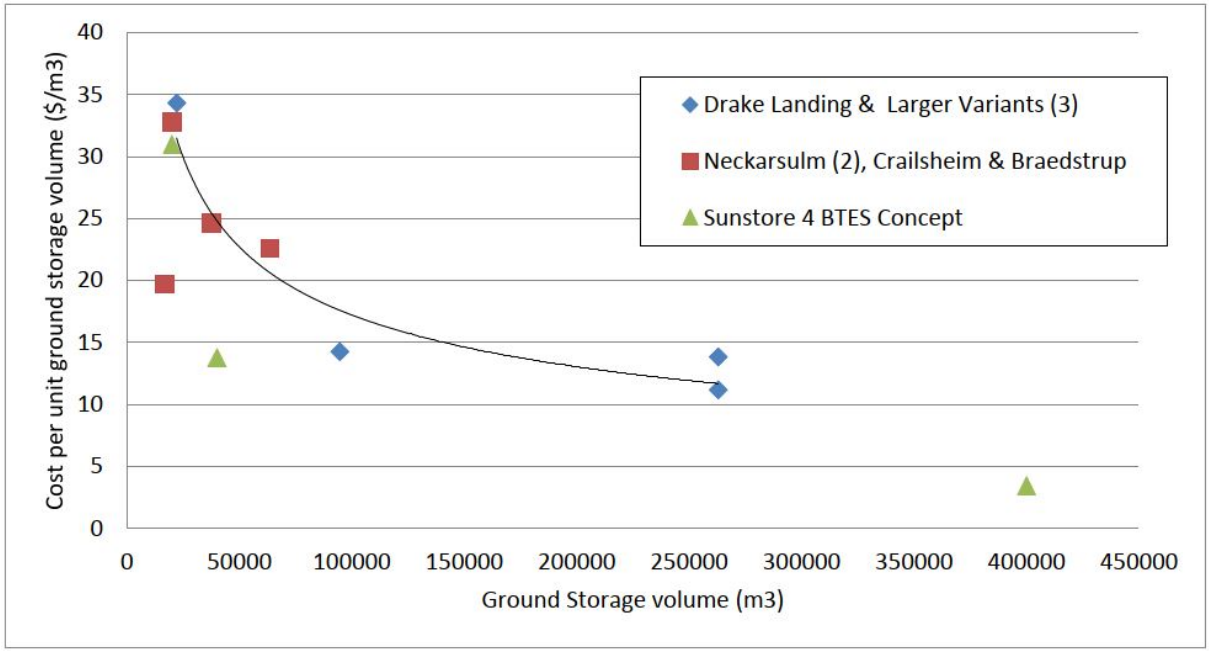

Figure 6.1: Specific cost for several BTES systems. Source: IRENA (2021)

The size of the studied BTES system would be over 1,000,000 m^3. This volume is not shown in the Figure 6.1, but extrapolating would result in unit price being less than 5 \$/m^3. Table 6.3 shows different CAPEX costs for the BTES.

Table 6.3: Estimated capital costs for the BTES.

Location	Unit Price	Cost [M€]	Source
Canada	116 \$/m	9.432	Rad et al. (2017)
-	5 €/m^3	11.025	IRENA (2021)
Norway	10 k€/BH	4.695	Asplan Viak

The values from IRENA (2021) and Rad et al. (2017) are circa two times the value discussed with the contractor during fieldwork. In the literature, the value is for the whole system, which also includes connection, possible heat pumps and energy center (with short term storage e.g. water tank). The value given by the contractor only includes drilling of the borehole and installation of the collector pipe. This mismatch would explain the price different between the sources.

6.3 Heat pumps and network

BTES is practically a geothermal heating-and-cooling system which operates with or without GSHP. For high temperature BTES heat pumps might not be needed since the temperature of outflowing fluid is at high temperature. However as the design of the model is based on having temperature difference close to 50 °C but not exceeding +50 °C, the result is that temperature at the end of discharging period drops to near single values. For this reason heat pumps are added as a component in the system. Also Gehlin (2016) discusses that even when BTES-HT does not require heat pumps, they can be added to improve system and reduce heat losses. Due to the high heat extraction and injection rates, a heat pump(s) are required to have high capacity, in the range of kilowatts per borehole. According to Hansen and Gudmundsson (2018) the capital cost of a heat pump with the capacity for providing heat transfer for one borehole is 20,000 € and O&M costs are 360 €/year.

6.4 Levelized Cost of Energy

To calculate the Levelized Cost of Energy (LCOE), CAPEX and OPEX are summed together and divided with the produced heat over the life cycle of the system. Due to inflation the

value of money in 20 years is lower than that of today. For this reason the future cashflows have to be discounted to represent value in todays currency. LCOE is calculated with discount rate of 5-8 %. Life cycle for most components within the system are 20-30 years.

$$LCOE = \frac{\sum_{t=1}^{n} \frac{I_t + M_t}{(1+r)^t}}{\sum_{t=1}^{n} \frac{E_t}{(1+r)^t}} \tag{6.1}$$

where:

I_t = Capital costs per year t [€]

M_t = O&M costs per year t [€]

E_t = Energy produced per year t [MWh]

r = Discount rate [%]

t = year [-]

n = system life [-]

Table 6.4 shows the chosen values for calculating the LCOE.

Table 6.4: Estimated CAPEX and OPEX cost for the whole system.

Component	CAPEX [M€]	OPEX [M€]
Solar collector	50	0.95
BTES	4.84	-
Heat pumps	9.68	1.742
SUM	64.520	1.124

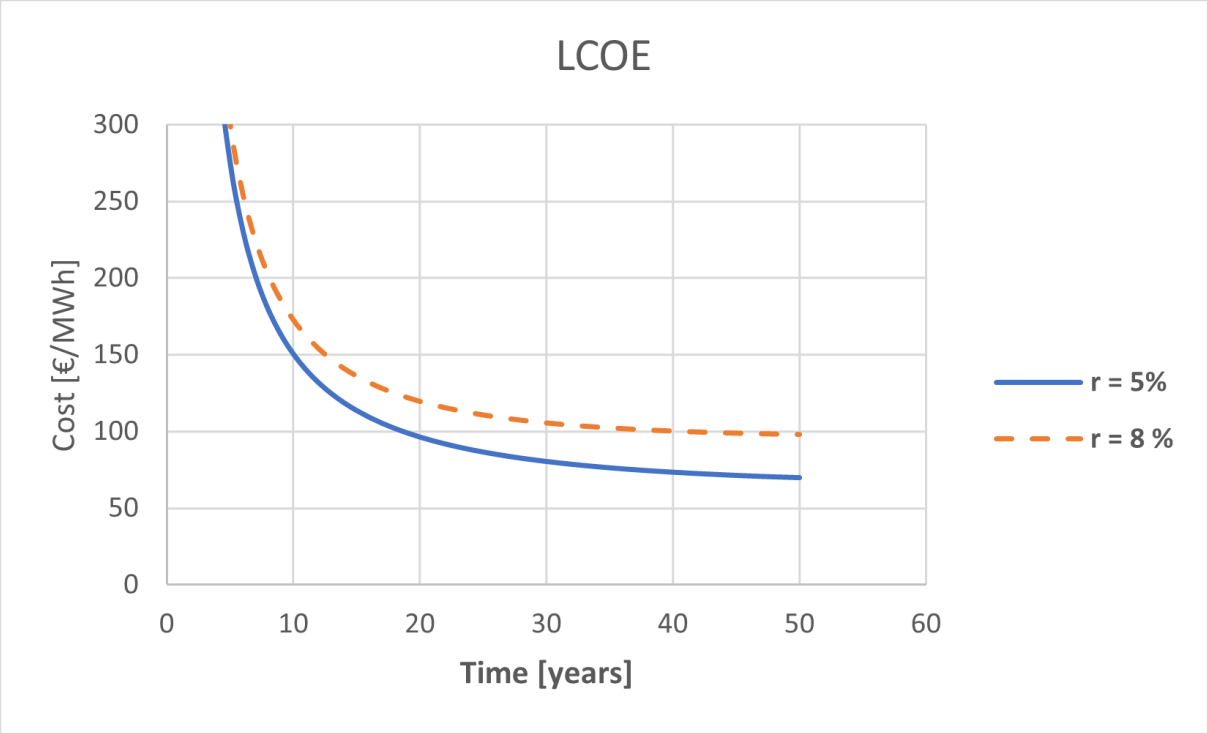

Figure 6.2: Levelized Cost of Energy as a function of system life time calculated with 5 and 8 % discount rate.

The curve in Figure 6.2 shows how the LCOE value lowers as a function of time. The longer the life time of the system, the lower LCOE is. The rapid drop in the LCOE shows that these types of system have high initial costs. With 5 % discount rate the LCOE is lower than 100 €/MWh at 20 years of operation. With 8 % discount rate it will take close to 40 year to reach this value. Figure 6.3 shows LCOE of heating for Austria, Germany and Mexico for comparison.

Figure 6.3: Levelized Cost of Heating time-series from Austria, Mexico and Germany. Source: IRENA (2021)

The LCOE of proposed BTES system in Longyearbyen is in the same magnitude as the price range shown in Figure 6.3. Until year 2019 the LCOE in Austria was above 100 €/MWh, where as the most recent data shows that is has dropped to to approximately 80 €/MWh

in 2020. LCOE in Germany has decreased from 2014 to 2016, after which it fluctuated at little over 100 €/MWh. Since 2018 the trend has been increasing, the cost being close to 150 €/MWh at 2020. Mexico shows the most stable and lowest LCOE for heating. Trend is slowly decreasing from 60 in 2010 to 40 €/MWh in 2020.

The LCOE calculated in Table 6.4 is preliminary estimate, and includes major uncertainties. This model does not take into account the depreciation of the system, nor does it consider any residual cost. Also no incentives have been taken into account. The aforementioned factors would lower the LCOE, thus making the system more economically feasible. However the CAPEX and OPEX costs of the system might be considerably higher in Svalbard due to isolation & remoteness and regional differences. Also electricity prices have not been directly added to the O&M costs. Even without heat pumps the system is relying on regular circulating pumps, which are powered by electricity. However these costs could be estimated to be embedded in the solar collector and heat pump O&M costs.

Chapter 7

Summary and Recommendations for Further Work

7.1 Summary and Conclusions

Field test results from near Longyearbyen indicates that the bedrock is suitable for BTES. Thermal conductivity of the bedrock is high and drillability is good. These factors are in favor of the constructing the BTES.

Simulations showed that the area around the BTES would thaw over tens of meters away from the peripheral boreholes. The extent of the permafrost thaw is less at the ground surface than in the depth of bedrock. This has to be taken into consideration. BTES is not recommended to be constructed near existing structures, such as the global seed vault which has the entrance approximately 600 meters away from the drill site 1.

The estimated LCOE for the whole system is near 100 €/MWh. However the calculations include a lot of uncertainties and many components of the cost structure were estimated at the higher range to get a more conservative value. The final conclusion is that the directive price estimate is at a reasonable range and forms a basis for future studies.

7.2 Discussion

As the results and discussion in the previous sections indicate, this study found no direct obstacles for implementing the BTES in the high Arctic. The cost of such a system would in the high end price range, but with incentives and subsidies it may be feasible.

One major concern is the methane gas observed during the drilling of the borehole (see section 4). Careful research should be made to study the source of the methane. Permafrost

is considered a barrier which witholds the carbon dioxide injected into the bedrock in the CO2 project. It appears to act in a similar way regarding the naturally occurring methane. Constructing a BTES would essentially thaw a hole with diameter up to hundred of meters into this gas trapping “plug”. Further investigations should be conducted to determine what would happen to the methane in this scenario.

TRT tests may require longer time in permafrost areas. The ground is frozen in the initial state, and starts to thaw as the TRT proceeds. Due to different thermal properties of frozen and unfrozen ground, the rate of heat conduction within the ground might differ as the thawing front propagates further, essentially affecting the results.

BTES should not be constructed near structures which depend on existing permafrost. However since the footprint of the BTES is relatively small (circa 100 x 100 meters) a feasible location should be easy to find.

Thermal conductivity of the GHE can be further increased by grouting the borehole. This also helps to mitigate the effects from possible groundwater flow. Additionally grouted boreholes do not have the risk of freezing and in the worst case breaking the collector tubes.

7.3 Recommendations for Further Work

The numerical model presented in this thesis is a simplified version of the reality. A more precise model is suggested to more precisely simulate the in-situ conditions. In COMSOL this would mean for example adding the actual fluid flow with predetermined temperature and flow rate into the boreholes.

Lot of samples were collected during the field work. Testing these samples for thermo-mechanical parameters would provide more in depth understanding of the subsurface. For example measuring thermal conductivity in a laboratory could provide more insight into the consistency of the bedrock. This could be used to verify the various layers discovered with the DTRT tests.

Bibliography

Acuña, J. (2013). *Distributed thermal response tests - New insights on U-pipe and Coaxial heat exchangers in groudnwater-filled boreholes.* PhD thesis, KTH.

Allard, M. and Lemay, M. (2012). *Nunavik and Nunatsiavut: From science to policy. An Integrated Regional Impact Study (IRIS) of climate change and modernization.* ArcticNet Inc., Quebec City, Canada.

Bany Mousa, O., Taylor, R. A., and Shirazi, A. (2019). Multi-objective optimization of solar photovoltaic and solar thermal collectors for industrial rooftop applications. *Energy Conversion and Management*, 195:392–408.

Borinaga-Treviño, R., Pascual-Muñoz, P., Castro-Fresno, D., and Blanco-Fernandez, E. (2013). Borehole thermal response and thermal resistance of four different grouting materials measured with a TRT. *Applied Thermal Engineering*, 53(1):13–20.

Braathen, A., Bælum, K., Christiansen, H. H., Dahl, T., Eiken, O., Elvebakk, H., Hansen, F., Hanssen, T. H., Jochmann, M., Johansen, T. A., Johnsen, H., Larsen, L., Lie, T., Mertes, J., Mørk, A., Mørk, M. B., Nemec, W., Olaussen, S., Oye, V., Rød, K., Titlestad, G. O., Tveranger, J., and Vagle, K. (2012). The Longyearbyen CO2 Lab of Svalbard, Norway — initial assessment of the geological conditions for CO2 sequestration. *Norwegian Journal of Geology*, 92:353–376.

Brekke, G. M., Møller-Holst, S., Sundseth, K., Ødegård, A., and Brekke, D. I. (2018). Fornybar energiforsyning til Svalbard - Longyearbyen. Report.

Bäcklund, A. S. (2009). *Analys av en grundvärmebaserad värmepumpsanläggning för uppvärmning och kylning av ett sjukhus.* PhD thesis, Norges teknisk-naturvitenskapelige universitet.

CIA World Factbook (2021). Physical Arctic Region. Available online: `https://www.cia.`

gov/the-world-factbook/static/a08caff80eeebcdc2d25b786b6de40f6/arctic_phy.jpg. Accessed on 28.06.2021.

Côté, J. and Konrad, J.-M. (2005a). A generalized thermal conductivity model for soils and construction materials. *Canadian Geotechnical Journal*, 42(2):443–458.

Côté, J. and Konrad, J.-M. (2005b). Thermal conductivity of base-course materials. *Canadian Geotechnical Journal*, 42(1):61–78.

Dai, L., Li, S., DuanMu, L., Li, X., Shang, Y., and Dong, M. (2015). Experimental performance analysis of a solar assisted ground source heat pump system under different heating operation modes. *Applied Thermal Engineering*, 75:325–333.

Dallmann, W. K. (2015). Geoscience Atlas of Svalbard. Report, The Norwegian Polar Institute.

Davis, N. (2001). *Permafrost: a guide to frozen ground in transition*. University of Alaska Press.

Dincer, I. and Rosen, M. A. (2011). *Thermal Energy Storage, Systems and Applications*. John Wiley et Sons, Ltd, 2 edition.

Dorval, J.-G. (2020). *Using local Svalbard rocks as a construction material*. PhD thesis, NTNU.

Edstedt, U. and Nordell, B. (1994). *Borrhålslager. Förutsättningar, Erfarenheter, Möjligheter*. Ljunglöfs Offset AB, Stockholm, Sweden.

Eisentraut, A. and Brown, A. (2014). HEATING WITHOUT GLOBAL WARMING Market Developments and Policy Considerations for Renewable Heat . Report, International Energy Agency.

Elvebakk, H. (2008). Results of borehole logging in CO2 wells, Dh1-CO2-07 and Dh2-CO2-07, Longyearbyen, Svalbard . Report 2008.054, Norwegian Geological Survey.

Epp, B. (2020). World's largest solar district heating plant with concentrating collectors.

Franco, A. and Conti, P. (2020). Clearing a Path for Ground Heat Exchange Systems: A Review on Thermal Response Test (TRT) Methods and a Geotechnical Routine Test for Estimating Soil Thermal Properties. *Energies*, 13(11).

Gao, L., Zhao, J., and Tang, Z. (2015). A Review on Borehole Seasonal Solar Thermal Energy Storage. *Energy Procedia*, 70:209–218.

Gehlin, S. (2016). *Borehole thermal energy storage*, pages 295–327. Elsevier Ltd.

Giordano, N. and Raymond, J. (2019). Alternative and sustainable heat production for drinking water needs in a subarctic climate (Nunavik, Canada): Borehole thermal energy storage to reduce fossil fuel dependency in off-grid communities. *Applied Energy*, 252.

GREBE (2017). Advice Notes on Solar Thermal Technology Economics for the NPA Region.

Hakala, P., Martinkauppi, A., Martinkauppi, Ilkka Leppäharju, N., and Korhonen, K. (2014). Evaluation of the Distributed Thermal Response Test (DTRT): Nupurinkartano as a case study. Report, Geological Survey of Finland.

Hansen, C. H. and Gudmundsson, O. (2018). The competitiveness of district heating compared to individual heating.

Harris, S. A., Brouchkov, A., and Guodong, C. (2018). *Geocryology Characteristics and Use of Frozen Ground and Permafrost Landforms*. Taylor & Francis Group, London, UK.

Harstad, A. O., Lyhdahl, A. O. K., and Frauenfelder, R. (2018). Vurdering av permafrost som geologisk barriere knyttet til deponietablering på Svalbard Delrapport 1 - Feltundersokelser og klimavurderinger. Report, NGI.

Hellström, G. (1991). *Ground heat storage : thermal analyses of duct storage systems*. PhD thesis, Mathematical Physics. Defence details Date: 1991-05-24 Time: 13:15 Place: Sektionen för teknisk fysik External reviewer(s) Name: [unknown], [unknown] Title: [unknown] Affiliation: [unknown] — The information about affiliations in this record was updated in December 2015. The record was previously connected to the following departments: Mathematical Physics (Faculty of Technology) (011040002), Department of Physics (011013000).

IRENA (2021). *Renewable Power Generation Costs in 2020*. International Energy Agency, Abu Dhabi.

Isaksen, K., Førland, E. J., Dobler, A., Benestad, R., Haugen, J. E., and Abdelkader, M. (2017). Klimascenarioer for Longyearbyen-området, Svalbard Delrapport 1, Statsbygg oppdrag: «Bygging og forvaltning på Svalbard i et langsiktig klimaperspektiv». Report, Norwegian Meteorological Institution.

Isaksen, K., Mühll, D. V., Gubler, H., Kohl, T., and Sollid, J. L. (2000). Ground Surface Temperature Reconstruction Based on Data from a Deep Borehole in Permafrost at Janssonhaugen, Svalbard. *Annals of Glaciology*, 31:287–294.

Jensen-Page, L., Loveridge, F., and Narsilio, G. A. (2019). Thermal Response Testing of Large Diameter Energy Piles. *Energies*, 12(14).

Johansen, O. (1975). *Thermal Conductivity of Soils*. PhD thesis, University of Trondheim.

Johnsson, J. (2017). *Winter Road Maintenance using Renewable Thermal Energy*. PhD thesis, Chalmers University of Technology.

Kilfrost (2021). Kilfrost GEO_TDS_EN6609_M, Technical Data Sheet. Available online: `https://www.muovitech.com/productdocs/EN_kilfrost_GEO_technical.pdf`. Accessed on 09.07.2021.

L. Gilbert, G., Instanes, A., O. Sinitsyn, A., and Aalberg, A. (2019). Characterization of two sites for geotechnical testing in permafrost: Longyearbyen, Svalbard. *AIMS Geosciences*, 5(4):868–885.

Lee, K. S. (2013). *Underground Thermal Energy Storage*. Green Energy and Technology. Springer.

Liebel, H. T. (2012). *Influence of Groundwater on Measurements of Thermal properties in fractured aquifers*. PhD thesis, Norwegian University of Science and Technology.

Mangold, D., Miedaner, O., Tziggili, E. P., Schmidt, T., Unterberger, M., and Zeh, B. (2012). Technisch-wirtschaftliche Analyse und Weiterentwicklung der solaren Langzeit; Forschungsbericht zum BMU-Vorhaben 0329607N.

Marcotte, D. and Pasquier, P. (2008). On the estimation of thermal resistance in borehole thermal conductivity test. *Renewable Energy*, 33(11):2407–2415.

Midttømme, K. (2017). Geotermisk energi - en del av framtidens energimiks for Longyearbyen? In *Fremtidens energiforsyning i Longyearbyen*.

Midttømme, K., Jochmann, M., Henne, I., Wangen, M., and Thomas, P. J. (2015). Is Geothermal Energy an Alternative for Svalbard? In *The Third Sustainable Earth Sciences Conference and Exhibition*.

Midttømme, K., Ramstad, R. K., Solli, A., Sørdal, T., and Elvebakk, H. (2004). Grunnvarmekartlegging i Asker og Bærum. Report, NGU.

Moen, T.-E. (2017). Kabel til Svalbard – utopi eller realisme? In *Fremtidens energiforsyning i Longyearbyen*.

Nielsen, K. (2003). Thermal Energy Storage A state-of-the-Art. Report, NTNU and SINTEF.

Nordell, B., Andersson, O., Rydell, L., and Liuzzo-Scorpo, A. (2015).

Norwegian Polar Institute (2021). TopoSvalbard. Available online: `https://toposvalbard.npolar.no/`. Accessed on 28.06.2021.

Nårstad, A., Borge, M. V., Nordhus, Ø. S., and Martinsen, K. (2018). Radisson Blu Polar Hotell, Longyearbyen – GEOTEKNISK GRUNNUNDERSØKELSER DATARAPPORT, APRIL. 2018. Report RIG-R01-A01, Sweco Norge AS.

Paul, N. (1996). *The Effect of Grout Thermal Conductivity on Vertical Geothermal Heat Exchanger Design and Performance*. Mechanical Engineering Department, South Dakota State University.

Pedersen, M. B. and Bæverfjord, M. G. (2018). Grunnundersøkelser Studentboliger Elvesletta. Report 1350027997, Rambøll Norge AS.

Rad, F. M., Fung, A. S., and Rosen, M. A. (2017). An integrated model for designing a solar community heating system with borehole thermal storage. *Energy for Sustainable Development*, 36:6–15.

Ramage, J., Jungsberg, L., Wang, S., Westermann, S., Lantuit, H., and Heleniak, T. (2021). Population living on permafrost in the Arctic. *Population and Environment*.

Ramstad, R. K., Midttømme, K., Liebel, H. T., Frengstad, B. S., and Willemoes-Wissing, B. (2014). Thermal conductivity cap of the Oslo region based on thermal diffusivity measurements of rock core samples.

Ratner, S., Gomonov, K., Revinova, S., and Lazanyuk, I. (2020). Energy Saving Potential of Industrial Solar Collectors in Southern Regions of Russia: The Case of Krasnodar Region. *Energies*, 13(4).

Raymond, J., Robert, G., Therrien, R., and Gosselin, L. (2010). A Novel Thermal Response Test Using Heating Cables. In *World Geothermal Congress 2010*.

Raymond, J., Therrien, R., Gosselin, L., and Lefebvre, R. (2011). A review of thermal response test analysis using pumping test concepts. *Ground Water*, 49(6):932–45.

Reuss, M. (2015). *The use of borehole thermal energy storage (BTES) systems*, pages 117–147. Woodhead Publishing.

Ringkjøb, H.-K., Haugan, P. M., and Nybø, A. (2020). Transitioning remote Arctic settlements to renewable energy systems – A modelling study of Longyearbyen, Svalbard. *Applied Energy*, 258.

Sanner, B., Hellström, G., Spitler, J., and Gehlin, S. (2005). Thermal Response Test - Current Status and World-Wide Application. In *World Geothermal Congress 2005*.

Skanska AB (2014). Entré Lindhagen, Sweden - Sustainability Case Study 122.

Solberg government (2021). Meld. St. 13 (2020 – 2021) Klimaplan for 2021– 2030 [White Paper]. Available online: `https://www.regjeringen.no/contentassets/a78ecf5ad2344fa5ae4a394412ef8975/nn-no/pdfs/stm202020210013000dddpdfs.pdf`. Accessed on 13.06.2021.

Souchez, R. A. and Lorrain, R. D. (1991). *Ice composition and glacier dynamics*. Springer-Verlag.

Stover, L. (2019). Reservekraftstasjon Longyearbyen Miljotekniske Grunnundersokelser Datarapport. Report, Ramboll.

Sun, T., Yang, L., Jin, L., Luo, Z., Zhang, Y., Liu, Y., and Wang, Z. (2020). A novel solar-assisted ground-source heat pump (SAGSHP) with seasonal heat-storage and heat cascade utilization: Field test and performance analysis. *Solar Energy*, 201:362–372.

The Norwegian Meteorological Institute (MET Norway) (2021). Weather observations for weather station Longyearbyen Airport SN99840. Available online: `https://seklima.met.no/observations/`. Accessed on 23.06.2021.

Time and Date AS (2021). Available online: `https://www.timeanddate.com/sun/norway/longyearbyen`. Accessed on 16.06.2021.

Vartdal, H. (2017). LNG basert infrastruktur i kombinasjon med solenergi. In *Fremtidens energiforsyning i Longyearbyen*.

Wawrzyniak, T., Osuch, M., Napiórkowski, J., and Westermann, S. (2016). Modelling of the thermal regime of permafrost during 1990–2014 in Hornsund, Svalbard. *Polish Polar Research*, 37(2):219–242.

Welsch, B., Rühaak, W., Schulte, D. O., Bär, K., and Sass, I. (2016). Characteristics of medium deep borehole thermal energy storage. *International Journal of Energy Research*, 40(13):1855–1868.

Witte, H. J. L., Gelder, G. J., and Spitler, J. D. (2002). In Situ Measurement of Ground Thermal Conductivity: A Dutch Perpective. *ASHRAE Transactions 2002*, 108.

Wold, M. (2015). Datarapport fra grunnundersokelser Bykaia, ORV og Hotellneset. Report, SWECO.

Xiong, J., Lin, H., Ding, H., Pei, H., Rong, C., and Liao, W. (2020). Investigation on thermal property parameters characteristics of rocks and its influence factors. *Natural Gas Industry B*, 7(3):298–308.

Yin, B. and Wu, X. (2018). Performance analysis on a large scale borehole ground source heat pump in Tianjin cultural centre. *IOP Conference series: Earth and Environmental Science*, 121.

NTNU
Norwegian University of
Science and Technology

DTU UNIS
The University Centre in Svalbard
Cold Climate
Engineering